Improved V_{cs} determination using precise lattice QCD form factors for $D \to K\ell\nu$

Bipasha Chakraborty,[1,*] W. G. Parrott,[2,†] C. Bouchard,[2] C. T. H. Davies,[2,‡] J. Koponen,[3] and G. P. Lepage[4]
(HPQCD collaboration)[§]

[1] *DAMTP, Centre for Mathematical Sciences, University of Cambridge, Wilberforce Road, Cambridge, CB3 0WA*
[2] *SUPA, School of Physics and Astronomy, University of Glasgow, Glasgow, G12 8QQ, UK*
[3] *Helmholtz Institute Mainz, Johannes-Gutenberg-Universität Mainz, 55099 Mainz, Germany*
[4] *Laboratory of Elementary-Particle Physics, Cornell University, Ithaca, New York 14853, USA*

(Dated: August 3, 2021)

We provide a 0.8%-accurate determination of V_{cs} from combining experimental results for the differential rate of $D \to K$ semileptonic decays with precise form factors that we determine from lattice QCD. This is the first time that V_{cs} has been determined with an accuracy that allows its difference from 1 to be seen. Our lattice QCD calculation uses the Highly Improved Staggered Quark (HISQ) action for all valence quarks on gluon field configurations generated by the MILC collaboration that include the effect of u, d, s and c HISQ quarks in the sea. We use eight gluon field ensembles with five values of the lattice spacing ranging from 0.15 fm to 0.045 fm and include results with physical u/d quarks for the first time. Our calculated form factors cover the full q^2 range of the physical decay process and enable a Standard Model test of the shape of the differential decay rate as well as the determination of V_{cs} from a correlated weighted average over q^2 bins. We obtain $|V_{cs}| = 0.9663(53)_{\rm latt}(39)_{\rm exp}(19)_{\eta_{EW}}(40)_{\rm EM}$, where the uncertainties come from lattice QCD, experiment, short-distance electroweak and electromagnetic corrections, respectively. This last uncertainty, neglected for $D \to K\ell\nu$ hitherto, now needs attention if the uncertainty on V_{cs} is to be reduced further. We also determine V_{cs} values in good agreement using the measured total branching fraction and the rates extrapolated to $q^2 = 0$. Our form factors enable tests of lepton flavour universality violation. We find the ratio of branching fractions for $D^0 \to K^-$ with μ and e in the final state to be $R_{\mu/e} = 0.9779(2)_{\rm latt}(50)_{\rm EM}$ in the Standard Model, with the uncertainty dominated by that from electromagnetic corrections.

I. INTRODUCTION

The flavour changing weak interactions between quarks via emission of W bosons can be parameterised in terms of the unitary Cabbibo-Kobayashi-Maskawa (CKM) matrix in the Standard Model, given by [1, 2]

$$V_{\rm CKM} = \begin{bmatrix} V_{ud} & V_{us} & V_{ub} \\ V_{cd} & V_{cs} & V_{cb} \\ V_{td} & V_{ts} & V_{tb} \end{bmatrix} . \quad (1)$$

Precise and independent determination of each of the CKM matrix elements from multiple processes is crucial to test the Standard Model stringently. Current accuracy varies from 0.014% for V_{ud} to 6% for V_{ub} with several reviews in [3] discussing different aspects of their determination. For a recent review of the impact of lattice QCD on this endeavour see [4]. Here we will focus on the determination of V_{cs} and provide a significant improvement in its accuracy that expands the range of tests we can perform of the CKM matrix.

Any significant deviation from unitarity of the CKM matrix would signal the existence of physics beyond the Standard Model, but the accuracy with which unitarity tests can be performed varies substantially across the matrix. The unitarity of the first row has been tested to a precision of 0.05%. A result of

$$|V_{ud}|^2 + |V_{us}|^2 + |V_{ub}|^2 = 0.9985(3)_{V_{ud}}(4)_{V_{us}} \quad (2)$$

is quoted in 'V_{ud}, V_{us}, the Cabibbo Angle and CKM Unitarity' in [3], noting that the value of V_{ub} is too small to affect this relation. V_{ud} here is determined from superallowed nuclear β decay with a 0.01% experimental accuracy that requires careful treatment of electroweak radiative corrections (see the review for a discussion of this). V_{us} is determined from a weighted average of results from combining experimental results for K meson leptonic and semileptonic decays with lattice QCD calculations of the appropriate hadronic parameters [5–7]. A determination with uncertainty better than 0.3% is possible in both cases, paying attention to various sources of electroweak radiative corrections. The value quoted in Eq. (2), with its 3σ hint of a discrepancy with unitarity, results from a weighted average of leptonic and semileptonic V_{us} values with an uncertainty increased by a factor of two to allow for the tension between them.

Tests of unitarity for other rows and columns of the CKM matrix are much less stringent, either because of larger experimental uncertainties, larger theoretical uncertainties or both. Our aim here is to improve V_{cs}. Since V_{cs} is close to 1 in value, it needs to have a small uncertainty to avoid ruining any CKM unitarity test that it appears in. The determination of V_{cs} proceeds most directly, as for V_{us}, either through a study of leptonic

* bc335@cam.ac.uk
† w.parrott.1@research.gla.ac.uk
‡ christine.davies@glasgow.ac.uk
§ http://www.physics.gla.ac.uk/HPQCD

decays of the D_s meson or through D semileptonic decay to $K\ell\nu$. We summarise its current status below before outlining our new determination.

We will not discuss the determination of V_{cs} from other semileptonic channels such as $D_s \to \phi$ [8] or $\Lambda_c \to \Lambda$ [9]. These are not currently competitive but do provide further checks on V_{cs}; the baryon channel is particularly important to provide constraints on new physics complementary to those available from meson decays.

A. Current situation on V_{cs}

The experimental measurement of the branching fraction for D_s leptonic decay has been challenging, with the average drifting downwards slowly with time as newer results are added. The current situation is reviewed in 'Leptonic decays of charged pseudoscalar mesons' in [3] (we will refer to this as RSV). See also results from the Heavy Flavor Averaging Group (HFLAV) [10]. There are now experimental results from BaBar, Belle, BES III and CLEO-c with either μ or τ in the final state. The experimental branching fraction $D_s \to \ell\overline{\nu}$ is obtained after removing the effect of QED bremsstrahlung at leading-log order using PHOTOS [11]. The measured width is then given by

$$\Gamma = \frac{G_F^2 m_\ell^2 M_{D_s}}{8\pi}(\eta_{EW} f_{D_s}|V_{cs}|)^2\left(1-\frac{m_\ell^2}{M_{D_s}^2}\right) \quad (3)$$

up to remaining QED effects (RSV apply a 1% correction to BaBar and Belle μ results to account for contamination from $D_s \to (D_s^* \to \ell\overline{\nu})\gamma$ [12]). η_{EW} accounts for short-distance electroweak corrections to the value of G_F obtained from the μ lifetime [13], a correction applied as standard in the K leptonic and semileptonic decays discussed above. The experimental width then yields a result for the combination $\eta_{EW} f_{D_s}|V_{cs}|$, where f_{D_s} is the decay constant of the D_s meson, the hadronic parameter that determines the amplitude for annihilation to a W boson. RSV take $\eta_{EW} = 1.009$ and obtain an average from experiment of

$$|V_{cs}| f_{D_s} = 245.7(3.1)(3.4)\ \text{MeV}. \quad (4)$$

The first error here comes from the experimental branching fractions and the second error takes a 100% uncertainty from the applied radiative corrections (η_{EW} and the additional 1% on the rate to μ above). The average from HFLAV [10] (included in the review 'CKM Quark-Mixing Matrix' in [3]) has a larger central value because they take $\eta_{EW} = 1$, and a smaller uncertainty since they do not include the second uncertainty above. The total experimental uncertainty then ranges from 1.3% from HFLAV [10] to 1.9% from Eq. (4).

Early full lattice QCD calculations [14] of the D_s decay constant were undertaken before the experimental results were obtained. They had rather large (6%) systematic uncertainties from discretisation effects associated with the relatively heavy c quark mass and uncertainties from matching the normalisation of the lattice representation of the $c\overline{s}$ weak current to that in the continuum. A step-change in accuracy was made possible by the development of HPQCD's Highly Improved Staggered Quark (HISQ) action [15]. This has good control of discretisation effects (going beyond $\mathcal{O}((ma)^2)$) and a partially conserved axial current relation that enables the decay constant to be absolutely normalised. HPQCD used this to obtain a 1% accurate result for f_{D_s} [16, 17] back in 2010. Combined with the higher experimental average for the branching fraction at that time it led to a V_{cs} result with a central value above 1. More recent results from the Fermilab/MILC collaboration [5] using HISQ give a 0.2% uncertainty on f_{D_s}. RSV then give a leptonic determination

$$|V_{cs}|_{\text{lept}} = 0.983(13)(14)(2) \quad (5)$$

where the first uncertainty is from experiment, the second from radiative corrections and the third from f_{D_s}. We see that the current picture for V_{cs} from leptonic decays is one in which the experimental uncertainty dominates that from lattice QCD (f_{D_s}), which is now almost negligible here. When radiative corrections are considered, as in RSV, they also have a sizeable uncertainty. The value obtained for V_{cs} is consistent with 1.

The situation with semileptonic $D \to K$ decays is somewhat different. Smaller experimental uncertainties have been available for some time but lattice QCD calculations are harder to do, with less accurate results to date. The hadronic quantities that parameterise the amplitude for the $c \to s$ transition within the meson are form factors, functions of the squared 4-momentum transfer, q^2, from the initial D to final K meson. The only form factor that contributes here, for light leptons in the final state, is the vector form factor, $f_+(q^2)$. Here we will improve substantially on previous lattice QCD uncertainties for the $D \to K$ form factor and demonstrate the improvement in accuracy of V_{cs} that results. This will inevitably mean, as discussed above, that uncertainties from electroweak radiative corrections will rear their heads.

Experimental results for $D \to K\ell\overline{\nu}$ are available from BaBar, Belle, BES III and CLEO-c [10] and will be discussed in more detail later. Results exist for both charged and neutral D mesons and with both e and μ in the final state. They are either given in the form of a differential distribution in bins of q^2 or, following a fit to the distribution combined with an analysis of radiative bremsstrahlung corrections using PHOTOS, a value for $\eta_{EW}|V_{cs}|f_+(0)$. HFLAV [10] quote an average for this latter quantity with a 0.5% uncertainty from experiment. Note that η_{EW} is taken to be 1 in these analyses and does not appear as a factor.

Full lattice QCD calculations of the $D \to K$ form factors again began before experimental results were available [18] but were limited in accuracy (to 10%) by systematic effects from the discretisation of the quark action. The use of the HISQ action by HPQCD brought

a big improvement [19] coupled with the fact that the scalar form factor f_0 (equal to f_+ at $q^2 = 0$) can be determined with absolute normalisation. HPQCD extended this to a determination of the vector form factor across the full physical q^2 range in [20] with nonperturbative normalisation of the vector current. This allowed a 1.6%-accurate determination of $|V_{cs}|$ using a bin-by-bin comparison of the differential distribution with experiment, thus providing also a Standard Model test of the shape of the distribution. Recently the European Twisted Mass Collaboration (ETMC) determined the full shape of the $D \to K$ form factors [21, 22] using the twisted mass formalism and combined that with experimental results to obtain a 3.5% accurate result for $|V_{cs}|$. Work is also underway by other groups; see, for example, [23, 24].

The ETMC result for $f_+^{D\to K}(0)$ is used in the 'CKM Quark-Mixing Matrix' review in [3] (quoting [7]) to give a semileptonic determination of V_{cs} as

$$|V_{cs}|_{\rm semi} = 0.939(38). \tag{6}$$

The uncertainty here is strongly dominated by that from lattice QCD. The result takes $\eta_{EW} = 1$ and does not include additional uncertainties to allow for possible missing QED corrections. Combining their results over the full range of q^2 with experiment, ETMC [22] instead obtains

$$|V_{cs}|_{\rm semi} = 0.978(35), \tag{7}$$

with similar uncertainty. Both results above are consistent with the value 1 within 2σ because of the large uncertainty. They also agree with the expectation $V_{cs} = V_{ud} = 0.97370(14)$ [3] to $\mathcal{O}((\lambda = V_{us})^4)$.

The results for $|V_{cs}|$ in Eqs (5), (6) and (7) contribute 4–7% uncertainties to CKM second row or column unitarity, i.e. two orders of magnitude worse than that for the first row discussed earlier (Eq. (2)). This precludes picking up hints of new physics.

Here we provide a substantial improvement to the lattice QCD determination of these form factors using the HISQ action on gluon field configurations that include u, d, s and c quarks in the sea. We build on [20] (although using a method for normalising the vector current suggested but not implemented there) to determine the scalar and vector form factor across the full physical q^2 range for the decay. This enables us to compare to experimental results in each q^2 bin as well as at $q^2 = 0$, as in [20–22], to determine V_{cs}. We include results over a larger range of lattice spacing values than in [20] and with sea light quark masses going down to physical values of the u/d mass. Our work will also provide form factors for the improved experimental determinations to come in future, for example from Belle II [25].

The paper is laid out as follows: Section II lays out our formalism and then Section III describes our lattice QCD calculation. This includes details of the gluon ensembles used and the correlation functions calculated followed by a description of how the calculated lattice correlation functions are fitted and values for the form factors extracted. We then describe how the form factor results are extrapolated to the physical continuum limit. Section III can be omitted by anyone who is not interested in the lattice QCD details. Section IV gives our results for the physical form factors, with instructions on how to reconstruct them from the parameters given. We compare the shape of the vector form factor to that obtained from the differential decay rate by experiment. We also give the ratio of branching fractions for a muon in the final state to that for an electron as a function of q^2 for tests of lepton flavour universality. Section V gives three different methods for determining V_{cs} using our results and experimental measurements of the $D \to K\ell\nu$ decay rate. Our preferred method is to use a bin-by-bin comparison with the differential decay rate but we also give values determined from the total branching fraction and from the rate at $q^2 = 0$. Section VI puts our improved results for V_{cs} into context with previous results and other CKM elements in tests of unitarity of the CKM matrix. Finally, Section VII gives our conclusions.

II. FORMALISM

We write the differential decay rate for $D \to K\ell\overline{\nu}$ (inclusive of photons) as:

$$\frac{d\Gamma}{dq^2} = \frac{G_F^2}{24\pi^3}(\eta_{EW}|V_{cs}|)^2(1-\epsilon)^2(1+\delta_{EM}) \times \left[|\vec{p}_K|^3(1+\frac{\epsilon}{2})|f_+(q^2)|^2 + |\vec{p}_K|M_D^2\left(1-\frac{M_K^2}{M_D^2}\right)^2\frac{3\epsilon}{8}|f_0(q^2)|^2\right] \tag{8}$$

where $\epsilon = m_\ell^2/q^2$, m_ℓ being the lepton mass, and $\vec{p}_K$ is the 3-momentum of the K in the D rest frame. Note that the contribution of f_0 to the differential rate is suppressed by ϵ. η_{EW} accounts for universal short-distance corrections to G_F from box diagrams in the Standard Model [13]. We take

$$\eta_{EW} = 1 + \frac{\alpha_{QED}}{\pi}\log\left(\frac{M_Z}{M_D}\right) = 1.009(2) \tag{9}$$

where the uncertainty allows for a factor of two variation in the lower scale from the central value of M_D. δ_{EM} accounts for QED corrections to the leading-order formula. Some of these corrections may be q^2-dependent. We will handle δ_{EM} by taking an overall uncertainty for it, rather than making an explicit correction (see Section V).

In Eq. (8) f_+ and f_0 are the vector and scalar form factors for the process, respectively. They are defined from the matrix element of the vector part of the weak current between D and K, since that is the only part that contributes for a pseudoscalar meson to pseudoscalar meson semileptonic decay. The parameterisation of the matrix element of the vector current, $V^\mu = \overline{\psi}_s\gamma^\mu\psi_c$, in the con-

tinuum can be written as

$$\langle K|V^\mu|D\rangle = f_+^{D\to K}(q^2)\left[p_D^\mu + p_K^\mu - \frac{M_D^2 - M_K^2}{q^2}q^\mu\right] + f_0^{D\to K}(q^2)\frac{M_D^2 - M_K^2}{q^2}q^\mu, \quad (10)$$

where M_D and M_K are the masses of the D and K mesons (charged or neutral, as appropriate) respectively. The momentum transfer, $q^\mu = p_D^\mu - p_K^\mu$.

Application of the partially conserved vector current (PCVC) relation shows that the scalar form factor can also be obtained from the matrix element of the scalar current, $S = \overline{\psi}_s\psi_c$:

$$\langle K|S|D\rangle = \frac{M_D^2 - M_K^2}{m_c - m_s}f_0^{D\to K}(q^2). \quad (11)$$

The PCVC relation also holds in lattice QCD for the HISQ discretisation [15] of the quark action that we use. This means that $(m_c - m_s)\langle K|S|D\rangle$ is not renormalised and f_0 is obtained from the HISQ lattice QCD calculation with absolute normalisation [19]. Eq. (10) requires that $f_+(0) = f_0(0)$ and hence a determination of the scalar form factor obtained at $q^2 = 0$ is sufficient to determine the vector form factor there. This can then be combined with experimental results, if they are given in the form of a determination of $|V_{cs}|f_+(0)$, to yield a value for V_{cs} [19]. We will make use of this as one method to obtain $|V_{cs}|$.

Here we also determine f_+ over the full range of physical q^2 for the decay so that we can compare to the differential rate from experiment using Eq. (8). Although the HISQ action has a conserved vector current that is well understood [26], it is a complicated operator with several different multilink point-split components. Instead we use here a much simpler local vector current but this must be renormalised to match the (partially) conserved current. We do this by writing $V^\mu = Z_V V^\mu_{\rm latt}$ and determine Z_V by comparing scalar and temporal vector matrix elements in the 'zero recoil' configuration where the D and K are both at rest and $q^2 \equiv q^2_{\rm max} = (M_D - M_K)^2$. Then, from Eq. (10)

$$Z_V\langle K|V^0_{\rm latt}|D\rangle = f_0^{D\to K}(q^2_{\rm max})(M_D + M_K) \quad (12)$$

so that Z_V can be determined at this kinematic point [20] from

$$(M_D - M_K)Z_V\langle K|V^0_{\rm latt}|D\rangle_{q^2_{\rm max}} = (m_c - m_s)\langle K|S|D\rangle_{q^2_{\rm max}}. \quad (13)$$

Note that m_c and m_s here are the HISQ lattice quark masses for c and s. This provides a self-consistent normalisation for the matrix elements in Eqs. (10) and (11) that matches that in the continuum.

III. LATTICE CALCULATION

A. Simulation details

The calculation used gluon ensembles generated by the MILC collaboration [30]. The gluon action is improved through $\mathcal{O}(\alpha_s a^2)$ [31] and includes the effect of four flavours of sea quarks ($N_f = 2 + 1 + 1$) using the HISQ action [15]. The u and d sea quark masses are taken to be the same, with value denoted $m_l^{\rm sea}$. The eight ensembles used have parameters listed in Table I. Sets 1, 2 and 3 have $m_l^{\rm sea}$ set to the physical average value of m_u and m_d, whilst sets 4-8 have $m_l^{\rm sea/val} = 0.2m_s^{\rm sea}$. These 'second-generation' gluon field configurations are a significant improvement over the 'first-generation' $N_f = 2 + 1$ Asqtad configurations used in [20]. We also have results for a bigger range of lattice spacing values and going down to smaller values, from $a = 0.15$ fm to $a = 0.045$ fm. Although [20] discussed the use of the local temporal vector current, the results were obtained using a one-link-split spatial vector current. We believe that the approach using the local temporal current that we adopt here gives improved statistical and systematic uncertainties.

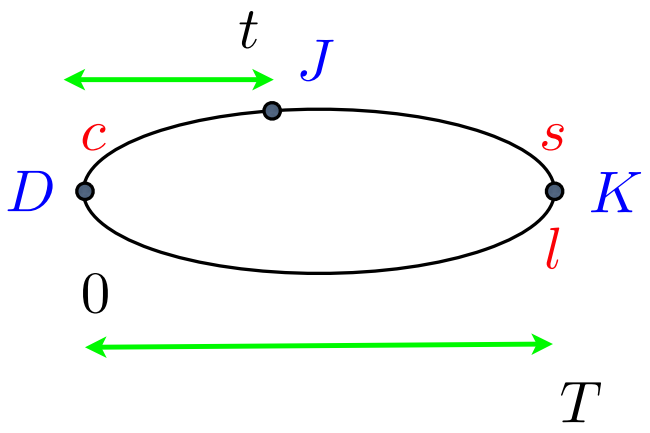

FIG. 1. Schematic diagram of our three-point correlation function for current insertion J.

B. Lattice correlation functions

Our goal is to extract scalar and temporal vector current matrix elements between D and K mesons for the determination of form factors using Eqs. (10) and (11). To do this we calculate three-point correlation functions on the lattice, as shown schematically in Figure 1, constructed by multiplying together three valence quark propagators, obtained by solving the Dirac equation on the gluon field configuration. We use propagators for a c quark, an s quark and a 'spectator' light quark, combined together with appropiate spins (implemented by a position-dependent phase for staggered quarks [15]) to give a pseudoscalar meson at each end and an appropriate current operator at J. For computational cost it is most convenient to perform the calculation in the following way: two of the propagators, s and l, are generated from the same random wall source and the third quark propagator, the c, is an extended propagator using as a source the appropriate timeslice of the light quark propa-

TABLE I. Parameters for the $N_f = 2+1+1$ gluon field configurations used in this work. The Wilson flow parameter [27] is used to determine the lattice spacing, a, via the values for w_0/a. We take $w_0 = 0.1715(9)$fm, as determined in [28] from f_π. Column 4 gives approximate values for a in fm for each set, and column 5 gives the approximate value for the ratio of the light quark mass to that of strange in the sea (the physical value is close to 0.036 [5]). Column 6 gives the spatial (N_x) and temporal (N_t) dimensions of each lattice in lattice units and column 7 the number of configurations and time origins used in our calculation. Columns 8–12 give the masses of the valence and sea quarks in lattice units. For the light (u/d) quark the valence and sea masses are the same. Column 13 shows values for the normalisation $Z_{\rm disc}$, defined in [29] and appearing in Eq. (22).

Set	β	w_0/a	a (fm)	$(m_l/m_s)^{\rm sea}$	$N_x^3 \times N_t$	$n_{\rm cfg} \times n_{\rm src}$	$am_l^{\rm sea/val}$	$am_s^{\rm sea}$	$am_c^{\rm sea}$	$am_s^{\rm val}$	$am_c^{\rm val}$	$Z_{\rm disc}$
1	5.8	1.1367(5)	0.15	0.036	$32^3 \times 48$	998×16	0.00235	0.0647	0.831	0.0678	0.8605	0.99197
2	6.0	1.4149(6)	0.12	0.036	$48^3 \times 64$	985×16	0.00184	0.0507	0.628	0.0527	0.643	0.99718
3	6.3	1.9518(7)	0.09	0.033	$64^3 \times 96$	620×8	0.00120	0.0363	0.432	0.036	0.433	0.99938
4	5.8	1.1119(10)	0.15	0.20	$16^3 \times 48$	1020×16	0.013	0.065	0.838	0.0705	0.888	0.99105
5	6.0	1.3826(11)	0.12	0.20	$24^3 \times 64$	1053×16	0.0102	0.0509	0.635	0.0545	0.664	0.99683
6	6.3	1.9006(20)	0.09	0.20	$32^3 \times 96$	499×16	0.0074	0.037	0.440	0.0376	0.449	0.99892
7	6.72	2.896(6)	0.06	0.20	$48^3 \times 144$	415×8	0.0048	0.024	0.286	0.0234	0.274	0.99990
8	7.0	3.892(12)	0.044	0.20	$64^3 \times 192$	375×4	0.00316	0.0158	0.188	0.0165	0.194	0.99997

TABLE II. Details of the T values and K meson momenta used on each ensemble. Momenta can be obtained from twist, θ, via $\theta = |a\vec{p}_K|N_x/(\sqrt{3}\pi)$, where N_x is the spatial dimension of the lattice, given in Table I.

Set	θ	T/a
1	0, 2.013, 3.050, 3.969	9, 12, 15, 18
2	0, 2.405, 3.641, 4.735	12, 15, 18, 21
3	0, 0.8563, 2.998, 5.140	14,17,20
4	0, 0.3665, 1.097, 1.828	9, 12, 15, 18
5	0, 0.441, 1.323, 2.205, 2.646	12, 15, 18, 21
6	0, 0.4281, 1.282, 2.141, 2.570	14, 17, 20
7	0, 1.261, 2.108, 2.946, 3.624	20, 25, 30
8	0, 0.706, 1.529, 2.235, 4.705	24, 33, 40

gator. In Figure 1 the $c\bar{l}$ pseudoscalar operator is placed at the origin and labelled by 'D', the ground-state meson in that channel. Likewise the $s\bar{l}$ operator at T is denoted by 'K'. We calculate correlation functions from multiple different values of the origin timeslice (averaged over before fitting) to improve statistical errors. We also use multiple values of the time separation between D and K, T, to improve the determination of the ground-state to ground-state matrix element. The T values are listed in Table II.

The extra 'taste' degree of freedom for staggered quarks leads to some technical complications when constructing our meson 3-point correlation functions. We need to combine pseudscalar operators for the mesons at 0 and T with either a scalar or temporal vector current operator at t. Staggered bilinears of different taste for a given spin are constructed with different point-splitting arrangements. Our preference is to use local operators because they are simple and most precise (since they do not incorporate gluon fields). A further advantage is that they have no tree-level discretisation errors. We then have to make sure that the three operators chosen have appropriate tastes; if not, the correlation function will be zero. The simplest way to test this is to write down the correlation function using naive quarks and apply the transformation to staggered quarks so that the correlation function factorises into a product of a color trace over a product of staggered quark propagators and a spin trace over a product of gamma matrices. The spin trace will be zero if tastes have been incorrectly combined [15].

This means that we must use two different operators for the $c\bar{l}$ pseudoscalar meson depending on whether the current in the three-point correlation function is a scalar, $S = \bar{\psi}_s 1 \otimes 1\psi_c$, or temporal vector, $V^0 = \bar{\psi}_s\gamma^0 \otimes \gamma^0\psi_c$. We give both operators here in their conventional 'spin-taste' notation. The fact that the spin and taste gamma matrices are the same means that they are both local (i.e. with ψ and $\bar{\psi}$ fields at the same point). The operators are implemented for staggered quarks simply using a position-dependent patterning of ± 1 instead of γ matrices. In both cases we use an $s\bar{l}$ pseudoscalar operator for the K meson of 'Goldstone' form, i.e. $\bar{\psi}_l\gamma^5 \otimes \gamma^5\psi_s$. For the D meson we can use this same form, $\bar{\psi}_l\gamma^5 \otimes \gamma^5\psi_c$, for correlation functions with the scalar current, since this is taste-singlet with a taste matrix of 1. Since the local temporal vector current has taste γ^0 we use a different, but still local, operator in its correlation functions. We distinguish this operator by denoting it by $\hat{D}$; $\hat{D} = \bar{\psi}_c\gamma^5\gamma^0 \otimes \gamma^5\gamma^0\psi_l$. We also calculate two point correlation functions for the Goldstone pseudoscalar K, and the Goldstone and non-Goldstone D bilinears detailed above. The D meson masses for the Goldstone and non-Goldstone operators will not be the same but differ by a taste-splitting which is a discretisation effect. These splittings are very small for heavy mesons such as the D [15, 30]. We demonstrate that for this calculation in Appendix A.

We take the D meson to be at rest and give spatial momentum to the K meson so that we can map out the dependence of the form factors on q^2. We do this by using twisted boundary conditions [32] for the s-quark propagator. The twist is taken equally in all three spatial directions to generate a momentum in the $(1,1,1)$ direction, minimising discretisation effects for a given value of $|\vec{p}_K|$. The twist angle, $\theta = |a\vec{p}_K|N_x/(\sqrt{3}\pi)$, where N_x is the spatial extent of the lattice in lattice units. Different values of momentum were chosen so as to cover the full physical range of momentum transfer, q, and the twists used are listed in Table II.

We summarise below how the two-point correlation functions are built from quark propagators, $g_q(x_t, x_0)$, of flavour q from point $x_0 = (0, \vec{x}_0)$ to point $x_t = (t, \vec{x}_t)$. The two-point correlators are labelled by the ground-state meson in that channel

$$C_D(t) = \frac{1}{4}\sum_{\vec{x}_0,\vec{x}_t} \langle \mathrm{Tr}[g_c^\dagger(x_t,x_0) g_l(x_t,x_0)]\rangle, \tag{14}$$

$$C_{\hat{D}}(t) = \frac{1}{4}\sum_{\vec{x}_0,\vec{x}_t} \langle (-1)^{\bar{x}_0^0+\bar{x}_t^0} \mathrm{Tr}[g_c^\dagger(x_t,x_0) g_l(x_t,x_0)]\rangle, \tag{15}$$

where $\bar{x}^\mu = \sum_{\nu\neq\mu} x^\nu$, and

$$C_K^{\vec{p}}(t) = \frac{1}{4}\sum_{\vec{x}_0,\vec{x}_t} \langle \mathrm{Tr}[g_s^{\theta\dagger}(x_t,x_0) g_l(x_t,x_0)]\rangle. \tag{16}$$

The factor of $1/4$ is the inverse of the number of staggered quark tastes. We sum over the spatial components of x_t and x_0; the sum for x_0 is implemented using a random wall source. The $\langle\rangle$ denotes the average over gluon field configurations in an ensemble and the trace is over colour. θ denotes the twist that gives spatial momentum to the s quark.

Three-point correlation functions are built similarly [33, 34] and labelled by the current operator

$$C_S^{\vec{p}}(t,T) = \frac{1}{4}\sum_{\vec{x}_0,\vec{x}_t,\vec{x}_T} \langle \mathrm{Tr}[g_c^\dagger(x_T,x_t) g_l(x_T,x_0) g_s^{\theta\dagger}(x_t,x_0)]\rangle, \tag{17}$$

$$C_{V^0}^{\vec{p}}(t,T) = \frac{1}{4}\sum_{\vec{x}_0,\vec{x}_t,\vec{x}_T} \langle (-1)^{\bar{x}_t^0+\bar{x}_T^0} \times \mathrm{Tr}[g_c^\dagger(x_T,x_t) g_l(x_T,x_0) g_s^{\theta\dagger}(x_t,x_0)]\rangle. \tag{18}$$

In the next section we discuss how we fit these two- and three-point correlation functions to determine the D to K matrix elements and hence form factors.

C. Correlator Fits

We perform a simultaneous multi-exponential fit to all of the two- and three-point correlation functions on each gluon field ensemble, using a standard Bayesian approach [35][1]. The fit form that we use for the two-point correlator for meson H is

$$C_H(t) = \sum_{i=0}^{N_{\rm exp}} \Big(|d_i^{H,n}|^2 \left(e^{-E_i^{H,n}t} + e^{-E_i^{H,n}(N_t-t)}\right) - (-1)^{t/a} |d_i^{H,o}|^2 \left(e^{-E_i^{H,o}t} + e^{-E_i^{H,o}(N_t-t)}\right)\Big), \tag{19}$$

where we include on the first line a tower of excited states of H of energy $E_i^{H,n}$ and amplitude $d_i^{H,n}$ above the ground state ($i=0$) generated by our lattice operator. Staggered quark operators also generate a tower of opposite parity states that oscillate in time and we also include such states in our fit (on the second line above) with their own amplitudes and energies, $d_i^{H,o}$ and $E_i^{H,o}$.

Likewise the fit form for three-point correlators for current J is:

$$\begin{aligned} C_J^{\vec{p}}(t,T) = \sum_{i,j=0}^{N_{\rm exp}} \Big(& d_i^{K,n} J_{ij}^{nn} d_j^{\overset{(\wedge)}{D},n} e^{-E_i^{K,n}t} e^{-E_j^{\overset{(\wedge)}{D},n}(T-t)} \\ & - (-1)^{(T-t)/a} d_i^{K,n} J_{ij}^{no} d_j^{\overset{(\wedge)}{D},o} e^{-E_i^{K,n}t} e^{-E_j^{\overset{(\wedge)}{D},o}(T-t)} \\ & - (-1)^{t/a} d_i^{K,o} J_{ij}^{on} d_j^{\overset{(\wedge)}{D},n} e^{-E_i^{K,o}t} e^{-E_j^{\overset{(\wedge)}{D},n}(T-t)} \\ & + (-1)^{T/a} d_i^{K,o} J_{ij}^{oo} d_j^{\overset{(\wedge)}{D},o} e^{-E_i^{K,o}t} e^{-E_j^{\overset{(\wedge)}{D},o}(T-t)} \Big). \end{aligned} \tag{20}$$

This includes the same towers of normal and oscillating states for K and D as those in two-point correlation functions. The only new parameters here are the three-point amplitudes, J_{ij}. To obtain these requires both two- and three-point correlator fits so that the J_{ij} can be separated from the d_i and d_j amplitudes.

The key parameters that we want to determine from these fits are the ground-state to ground-state amplitudes, J_{00}^{nn}, for the lattice temporal vector and scalar currents. We include the tower of excited states to remove contamination of excited states from the ground-state parameters and so that systematic errors from this contamination are fully included in the uncertainties on the ground-state parameters. Discarding data for $t < t_{\rm min}$ allows us to fit a finite number, $N_{\rm exp}$, of excited states, and $t_{\rm min}/a$ takes values in the range 2 to 5 for different correlators and different lattice spacings. Our fits use $N_{\rm exp}$ of 4 ($a = 0.15$ fm and 0.12 fm lattices) and 5 (finer lattices).

Our fits use log-normal parameters to ensure non-negative amplitudes d_i (because all of our two-point correlators have the same operator at source and sink) and energy differences between ordered states. We estimate priors for the ground state energies and amplitudes using the effective mass and effective amplitudes, as in [34],

[1] We use the corrfitter package [36–38] to do this.

and give each a broad uncertainty (typically 5%), ensuring that the final result of the fit is much more precisely determined (by at least an order of magnitude) than this prior. The ground-state energy in the oscillating channel is taken to be 0.4 GeV above the ground-state D meson in the D correlator and 0.25 GeV above the ground-state K meson in the K channel, using information from the Particle Data Tables [3]. The prior widths are typically taken as 20% of the energy for the oscillating ground-state, again many times broader than the output from the fit. Likewise the priors for the ground-state to ground-state J^{nn}_{00} are estimated from the three-point correlators by dividing through by the relevant two-point correlators and multiplying by their effective amplitudes. These priors are given an uncertainty of 20-50% depending on the ensemble, again many times larger than the result from the fit.

For the K mesons with non-zero momentum, we take priors for the ground-state energy and amplitude based on the priors for the zero-momentum parameters and the dispersion relation. Denoting the prior for parameter x as $\mathcal{P}[x]$ we use

$$\mathcal{P}[aE^K_{0,\vec{p}}] = \sqrt{(\mathcal{P}[aE^K_{0,\vec{0}}])^2 + (a\vec{p})^2}\left(1 + \mathcal{P}[A]\left(\frac{a\vec{p}}{\pi}\right)^2\right),$$
$$\mathcal{P}[d^K_{0,\vec{p}}] = \frac{\mathcal{P}[d^K_{0,\vec{0}}]}{(1 + (\vec{p}/\mathcal{P}[E^K_{0,\vec{0}}])^2)^{1/4}}\left(1 + \mathcal{P}[B]\left(\frac{a\vec{p}}{\pi}\right)^2\right). \tag{21}$$

We take priors for A and B as 0 ± 1.

Priors for energy splittings between excited states are taken as 0.5 GeV with a 50% uncertainty. Priors for excited state non-oscillating and all oscillating amplitudes are based on the size of ground-state amplitudes and generally given 100% uncertainties. These are listed in Table V in Appendix A along with the priors for the remaining J^{kl}_{ij}.

Since we have many correlators on each gluon field ensemble, the covariance matrix that must be inverted to minimise χ^2 in our fits is very large. For a finite number of samples (gluon field configurations) there is a bias in the small eigenvalues of the covariance matrix that needs to be addressed in order to avoid underestimating uncertainties on the fit parameters; see Appendix D of [39] for a discussion of this. We address this bias by applying a singular value decomposition (svd) cut on the eigenvalues using tools provided in our fitting package [36] for estimating an appropriate value. Using an svd cut leads to an artificial reduction in the χ^2 value and so we implement additional 'svd-noise' [36, 39] for a more reliable χ^2 value. Our fit results are all based on fits for which this χ^2/dof value is less than or close to 1.

The results for the ground-state parameters for our preferred fits are given in Table VI in Appendix A.

Figure 2 shows an example of tests of the stability of our correlator fits against a variety of changes. These tests are performed on all of our fits. We give further tests of our fit results in Appendix A.

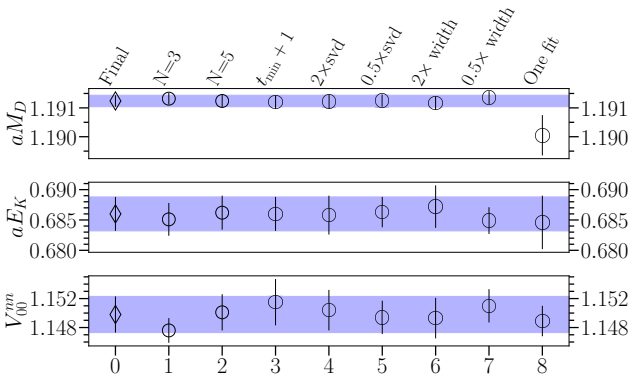

FIG. 2. Stability plot for our fit on the set 5 ($a = 0.12$ fm) lattice, with our preferred fit using $N = 4$ exponentials, shown as the value at location 0. The different panels show (from the top) the mass of the D (parameter $E_0^{D,n}$), the ground state energy of the K (parameter $E_0^{K,n}$) with the largest twist for this set of 2.646, and current matrix element for the temporal vector current V^{nn}_{00} (parameter J^{nn}_{00}) for twist 0.441. Tests 1 and 2 give the results from including one fewer and one more exponential respectively. Test 3 increases $t_{\rm min}/a$ by 1 across the whole fit. Tests 4 and 5 double and halve the svd cut and tests 6 and 7 double and halve all prior widths. The final test, 8, shows the results when the single correlator is fit on its own or, in the case of V^{nn}_{00}, just with the D and K two-point correlation functions required, rather than as part of one big simultaneous fit.

Our fit results for the three-point amplitudes J^{nn}_{00} are converted into the matrix elements we need in the following way:

$$\langle K|\, J\, |\overset{(\wedge)}{D}\rangle = 2Z_{\rm disc}\sqrt{M_D E_K}\, J^{nn}_{00}, \tag{22}$$

where M_D is the Goldstone D meson mass and E_K the K meson energy from the fit. We correct the normalisation for discretisation effects using the results of [29]. $Z_{\rm disc}$ differs from 1 at $\mathcal{O}((am_c)^4)$ which is less than 1% in all cases here; the values are given in Table I. For the temporal vector current the matrix element obtained above is $\langle K|\, V^0_{\rm latt}\, |\hat{D}\rangle$. This needs to be normalised by multiplication by Z_V, which is determined using the matrix elements at zero-recoil and Eq. (13). The Z_V values we obtain are listed in Table VI in Appendix A.

The vector and scalar form factors can now be determined from the matrix elements for the temporal vector and scalar currents on each gluon field ensemble using Eqs. (10) and (11). Our results for the form factors are listed in Table VI in Appendix A and plotted against q^2 in Figure 3. Little dependence on lattice spacing or sea light quark masses is visible. There are correlations between form factor values on a given field ensemble and these are captured in our correlator fits and passed on to the next stage of fitting. These correlations are sizeable between results for a given form factor (f_+ or f_0) at small values of the spatial momentum, close to zero-recoil. They are also substantial between f_+ and f_0 at

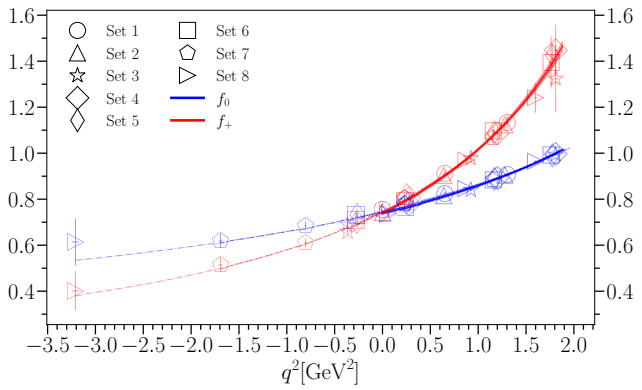

FIG. 3. f_0 and f_+ results on each of the 8 ensembles, marked by symbols as given in the legend. Our results cover the full physical q^2 range from $q^2 = 0$ to $q^2 = (M_D - M_K)^2 = 1.88\,\mathrm{GeV}^2$. The solid blue and red curves correspond to our fit results for the form factors in the continuum limit, as described in Section III D.

large values of spatial momentum close to $q^2 = 0$.

In the next section we discuss how we extrapolate our form factor results as a function of q^2 to the continuum limit.

D. Evaluating form factors at the physical point

Our results for the form factors at each value of q^2 on a given gluon field ensemble differ from the physical curve of $f(q^2)$ by discretisation effects and the mistuning of valence and sea quark masses. By fitting our results at multiple values of the lattice spacing and for multiple sea quark masses and allowing for valence quark mass mistuning we can account for both of these systematic effects. At the same time we interpolate in q^2 to obtain the physical form factor curves for the full kinematic range of q^2 values.

Our preferred method for doing this is to extend the form factors to an analytic function in the complex q^2-plane and then map the physical region into a line inside the unit circle in z-space. This enables a simple fit and $a \to 0$ extrapolation in z-space and we can then transform back to q^2. We will describe that approach first in Section III D 1, along with a variety of tests of its robustness. In Section III D 2 we will compare results to a direct cubic spline fit in q^2-space.

1. *Using a z-expansion*

The physical region of q^2 values for the $D \to K$ form factors is from $q^2 = 0$ to $q^2_{\mathrm{max}} = (M_D - M_K)^2$. In the larger complex $t = q^2$ plane we expect a branch cut to appear from $t = t_+ = (M_D + M_K)^2$ upwards, corresponding to DK production in the crossed channel. Since $M_D + M_K$ has the value 2.36 GeV, we also have two poles below $M_D + M_K$ in this channel, corresponding to the vector D_s^* meson and the scalar D_{s0}^*. We can map the cut-t plane into the interior of the unit circle in z-space using a standard mapping (see, for example [40]):

$$z(q^2, t_0) = \frac{\sqrt{t_+ - q^2} - \sqrt{t_+ - t_0}}{\sqrt{t_+ - q^2} + \sqrt{t_+ - t_0}}. \qquad (23)$$

Here t_0 is the point mapping on to $z = 0$. We take $t_0 = 0$ for simplicity but will show below that we get the same result using other values of t_0.

Since the form factor, with sub-threshold poles removed, is analytic we can fit to a polynomial form in z-space, modified by terms to allow for lattice discretisation and quark mass-mistuning effects [20]. We use the

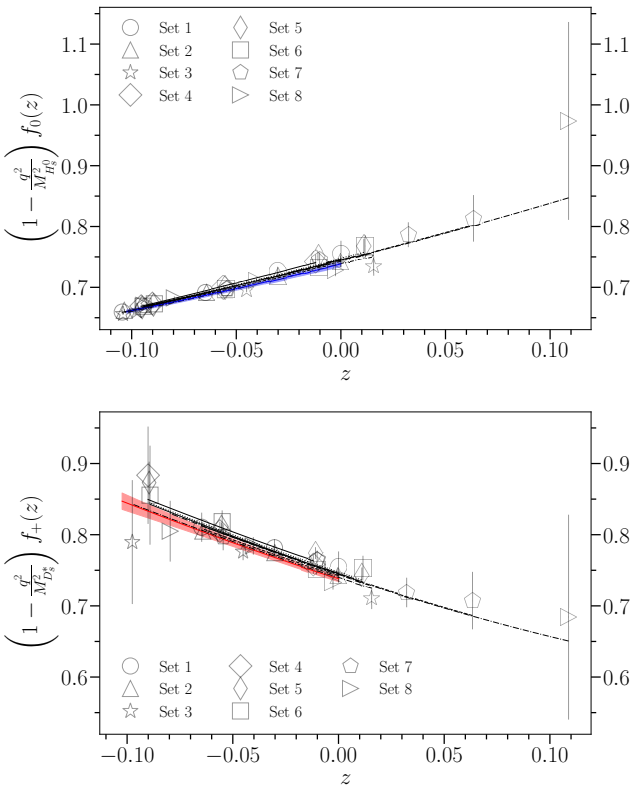

FIG. 4. Our lattice results for f_0 and f_+ on each of the 8 ensembles, plotted as a function of z (Eq. (23)). In both cases the expected pole has been removed. The points plotted then correspond to the left-hand side of Eq. (24). The solid blue and red curves correspond to the fit described in the text evaluated in the continuum limit and with quark masses tuned to their physical values. The curves are plotted for the range in z corresponding to the physical range in q^2. The black dashed lines give the fit results evaluated for each set of gluon field configurations.

Bourreley-Caprini-Lellouch (BCL) parameterisation [41],

$$(1-\frac{q^2}{M^2_{D^*_{s0}}})f_0(q^2) = (1+L(m_l))\sum_{n=0}^{N-1} a^0_n z^n \quad (24)$$
$$(1-\frac{q^2}{M^2_{D^*_{s}}})f_+(q^2) = (1+L(m_l))\times \sum_{n=0}^{N-1} a^+_n\Big(z^n - \frac{n}{N}(-1)^{n-N}z^N\Big).$$

We now describe each piece of this fit form in turn.

The factors of $1-q^2/M^2$ on the left-hand side of Eq. (24) remove the sub-threshold poles in the scalar and vector channels discussed above. The physical masses of the two mesons that appear are well known from experiment [3]. It is convenient in our calculation to use pole masses that are related to our D meson masses to minimise uncertainties from the lattice spacing. We therefore use two simple formulae for the pole masses in Eq. (24):

$$M_{D^*_{s0}} = M_D + \Delta_0; \quad (25)$$
$$M_{D^*_{s}} = M_D + \Delta_1\,,$$

where $\Delta_0 = M^{\rm phys}_{D^*_{s0}} - M^{\rm phys}_D$ and $\Delta_1 = M^{\rm phys}_{D^*_{s}} - M^{\rm phys}_D$ using mass values from [3]. $M^{\rm phys}_D$ is the average of the experimental masses for D^+ and D^0. The M_D values in Eq. (25) correspond to those from our lattice QCD calculation and the Δ values are constructed so that the pole masses in Eq. (24) are equal to the appropriate experimental masses when our lattice results are extrapolated to the physical point.

Figure 4 shows our results for the form factors with poles removed (i.e. the left-hand side of Eq. (24)) as a function of z. We can see that the z-dependence is very benign, almost linear with opposite sign gradients for f_+ and f_0, and there are no large deviations for discretisation effects or mistuning of sea quark masses. This enables a simple fit in z-space.

On the right-hand side of Eq. (24) we have a polynomial expansion in z multiplied by a term that includes a chiral logarithm, a function of the light quark mass. We discuss the logarithmic term below but first describe the polynomial expansion. We include N powers of z starting from z^0 and take each coefficient to be of the form

$$a^{0,+}_n = (1+\mathcal{N}^{0,+}_n)\times\sum_{j=0}^{N_j-1} d^{0,+}_{jn}\Big(\frac{am^{\rm val}_c}{\pi}\Big)^{2j}. \quad (26)$$

We take $N = N_j = 3$ for our preferred fit and will show below that our fits are stable to a change in the number of terms. Eq. (26) allows for discretisation effects in the coefficients of the z-expansion when j is non-zero. For the HISQ action, discretisation effects appear as even powers of the inverse lattice cut-off a/π. We allow for discretisation effects that are set by the charm quark mass m_c since that is the largest energy scale here. The coefficients that set the discretisation effects, $d^{0,+}_{jn}$ for $j>0$ take independent values for different values of n to allow for z-dependent (q^2-dependent) discretisation effects. They also take independent values for f_+ and f_0. In the absence of discretisation effects we have the kinematic constraint that $f_+(0) = f_0(0)$. Since we are using $t_0 = 0$, we can easily enforce this constraint by setting $d^+_{00} = d^0_{00}$.

The $\mathcal{N}^{0,+}_n$ term encodes (non-logarithmic) dependence on quark masses, again with independent coefficients for each value of n.

$$\begin{aligned}\mathcal{N}^{0,+}_n \quad &= c^{{\rm val},0,+}_{s,n}\delta^{\rm val}_s + c^{{\rm val},0,+}_{l,n}\delta^{\rm val}_l \\ &+ c^{{\rm sea},0,+}_{s,n}\delta^{\rm sea}_s + 2c^{{\rm sea},0,+}_{l,n}\delta^{\rm sea}_l \\ &+ c^{0,+}_{c,n}\Big(\tfrac{M_{\eta_c}-M^{\rm phys}_{\eta_c}}{M^{\rm phys}_{\eta_c}}\Big). \end{aligned} \quad (27)$$

In the first four terms,

$$\delta_q = \frac{m_q - m^{\rm tuned}_q}{10 m^{\rm tuned}_s} \quad (28)$$

takes account of the mistuning of the light and strange valence and sea quarks, relative to the tuned s quark mass. Dividing by $m^{\rm tuned}_s$ makes this a physical, scale-independent, ratio and the factor of 10 matches this approximately to the usual expansion parameter in chiral perturbation theory. We tune the m_s mass using the mass of the artificial $s\bar{s}$ pseudoscalar meson, the η_s, whose mass can be determined in terms of those of the π and K mesons in lattice QCD [28, 42]. $m^{\rm tuned}_s$ is obtained on each ensemble from [43]

$$m^{\rm tuned}_s = m^{\rm val}_s\left(\frac{M^{\rm phys}_{\eta_s}}{M_{\eta_s}}\right)^2, \quad (29)$$

with $M^{\rm phys}_{\eta_s} = 0.6885(20)$ GeV [28]. We then determine the tuned l quark mass from this using [5]

$$\frac{m^{\rm tuned}_s}{m^{\rm tuned}_l} = 27.18(10). \quad (30)$$

The final term in Eq. (27) allows for mistuning of the valence c quark mass. We take $M^{\rm phys}_{\eta_c}$ equal to 2.9766 GeV, allowing for the fact that the η_c mass determined from quark-line connected diagrams (only) on the lattice differs from the experimental value [3] by 7 MeV [44].

Returning to Eq. (24), the first term on the right-hand side allows for the chiral logarithms expected from hard pion chiral perturbation theory [45]. Following [46] we include a chiral logarithm term multiplying the polynomial in z for both f_+ and f_0. Because our light quark masses are small (with maximum $m_l/m_s = 0.2$) the K meson mass changes very little between different values of m_l. We therefore only include the chiral logarithm associated with the π meson mass:

$$L(m_l) = -\frac{9g^2}{8}x_\pi\Big(\log x_\pi + \delta_{FV}\Big), \quad (31)$$

where $x_\pi = M^2_\pi/\Lambda^2_\chi$, with Λ_χ the chiral scale of $4\pi f_\pi$. We rewrite x_π in terms of quark masses as $m_l/(5.63m^{\rm tuned}_s)$,

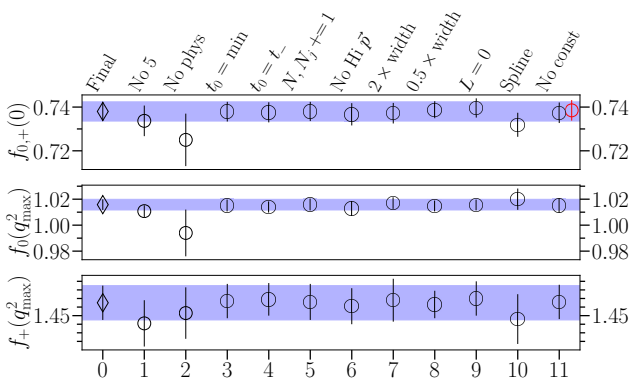

FIG. 5. Stability test of the z-expansion fit; 0 marks our final result. Test 1 removes all the results from gluon field configurations with $m_s/m_l = 5$, so that only sets 1, 2 and 3 remain. Test 2 removes the results from sets 1, 2 and 3 and fits the others. Test 3 takes t_0 in the q^2 to z mapping to the 'minimum' prescription described in the text. Test 4 sets t_0 to t_-. Test 5 includes an extra term in the sums over n up to N and over j up to N_j (Eqs. (24) and (26)). Test 6 removes the highest momentum data point for each gluon field ensemble (and highest two on set 7 so that there are no results included with $q^2 < 0$). Test 7 doubles the width of all 'd' priors (this decreased the Gaussian Bayes Factor), and 8 halves them. Test 9 sets the logarithmic factor $L(m_l)$ to zero (Eq. (31)). Test 10 shows the results of a completely different kind of fit, a cubic spline fit in q^2 discussed in Section III D 2. Test 11 removes the $f_0(0) = f_+(0)$ constraint, in this case the black point is $f_0(0)$ and the red is $f_+(0)$.

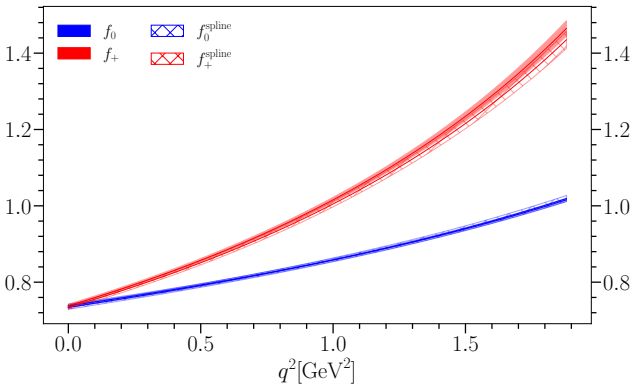

FIG. 6. A comparison of the f_+ and f_0 form factors, at the physical point ($a = 0$ and physical quark masses), obtained from our preferred z-expansion fit of Section III D 1 and from a cubic spline fit in q^2 of Section III D 2.

using the ratio of Λ_χ to M_{η_s} to evaluate the chiral logarithm accurately. δ_{FV} above is a finite-volume correction, calculated for each ensemble at the pion mass (See Eq.(47) of [47]). δ_{FV} has negligible effect in our fit. We take the $DD^*\pi$ coupling, $g = 0.570(6)$ from [48]. As shown in Eq. (27) we include other terms in our fit, independently for each z-expansion coefficient, to allow for (analytic) dependence on m_l from chiral perturbation theory. Our fit is not able to distinguish between linear and logarithmic dependence and so, as we will show below, gives the same result if the chiral logarithm of Eq. (31) is dropped. We include it in our preferred fit, however.

The priors on the d_{0n} in Eq. (26) that give the z-expansion coefficients in the continuum limit are taken to be 0 ± 2. All other d coefficients, that set the discretisation effects, are given prior 0 ± 1. The c coefficients in Eq. (27) that account for valence mass mistuning are given priors 0 ± 1; those that correspond to the smaller sea quark mass effects are given prior 0 ± 0.5. An Empirical Bayes study [35] suggests that our priors are conservative.

Our preferred fit, as described above, returns a χ^2/dof of 0.67 with 64 degrees of freedom. The stability of this fit against a variety of changes is demonstrated in Figure 5. We show the impact of omitting sets of lattice results, changing the numbers of terms in the z-expansion and the number of discretisation effects considered as well as doubling and halving the prior widths on all of the d coefficients. Modifications to the fit in which we drop the logarithmic term of Eq. (31) or remove the constraint that $f_+(0) = f_0(0)$ are tested. We also show the impact of changing t_0 from zero to the choice $t_0 = t_+\left(1-\sqrt{1-\frac{t_-}{t_+}}\right)$, which minimises the maximum magnitude of z as well as the choice $t_0 = t_- \equiv (M_D - M_K)^2$. In both of these two cases we implement the constraint that $f_+(0) = f_0(0)$ by setting the difference between them equal to a parameter with prior $0 \pm 1 \times 10^{-6}$. These two different values of t_0 correspond to different ranges for the fit in z-space with the q^2 distribution mapped very differently into z-space. The good agreement is a strong validation of the z-expansion approach. In Section III D 2 we consider a completely different kind of fit, to cubic splines in q^2 space, and compare the results of that also in Figure 5. Our fit result is stable against all of these changes, although the uncertainties increase significantly if the lattice results for physical m_l values (sets 1, 2 and 3) are dropped. Dropping all of the lattice results for the unphysical m_l values (sets 4–8) also increases the uncertainties but to a lesser extent. Note that dropping specific single lattices makes very little difference; the finest lattices (set 8) have almost no impact on the fit result.

In the next section we compare our z-expansion fit to a fit in q^2-space using cubic splines.

2. *Using a cubic spline in q^2*

There are choices to be made in implementing a z-expansion, from the choice of t_0 in the q^2 to z mapping to the prefactors in front of the polynomial in z (compare the form we use in Eq. (24) to that used for the shape parameters in Eq. (36)). Here, since we have precise lattice

QCD results over the full q^2 range of the decay, we can test a completely model-independent approach to the fit. Using cubic splines allows us to fit a very general function directly in q^2 space. We use the Steffen spline [49] to do this and denote each spline function, $g_i(q^2)$. After removing the expected pole, as described in Section III D 1, and including the chiral logarithm term of Eq. (31), we use a spline function g_0 to describe the physical dependence of each form factor on q^2 and further spline functions to account for discretisation and quark mass mistuning effects. The fit forms are given by:

$$(1-\frac{q^2}{M^2_{D^*_{s0}}})f_0(q^2) = (1+L(m_l))\times \left(g_0^0(q^2)+\sum_{j=1}^{N_j-1}\left[g_j^0(q^2)\left(\frac{am_c}{\pi}\right)^{2j}+\mathcal{N}^0\right]\right); \quad (32)$$

$$(1-\frac{q^2}{M^2_{D^*_{s}}})f_+(q^2) = (1+L(m_l))\times \left(g_0^+(q^2)+\sum_{j=1}^{N_j-1}\left[g_j^+(q^2)\left(\frac{am_c}{\pi}\right)^{2j}+\mathcal{N}^+\right]\right).$$

We take $N_j = 2$ but taking $N_j = 3$ gives no significant difference. For $\mathcal{N}$ we use further spline functions:

$$\begin{aligned}\mathcal{N}^{0,+} &= g_s^{\mathrm{val},0,+}\delta_s^{\mathrm{val}} + g_l^{\mathrm{val},0,+}\delta_l^{\mathrm{val}} \\ &+ g_s^{\mathrm{sea},0,+}\delta_s^{\mathrm{sea}} + 2g_l^{\mathrm{sea},0,+}\delta_l^{\mathrm{sea}} \\ &+ g_c^{0,+}\left(\tfrac{M_{\eta_c}-M_{\eta_c}^{\mathrm{phys}}}{M_{\eta_c}^{\mathrm{phys}}}\right).\end{aligned} \quad (33)$$

The definitions of δ_l and δ_s are given in Eq. (28).

All of the spline functions use the same four knots, positioned at q^2 values at either end of our range of results and with two values in between. This gives knot positions at {-3.25, -1.5, 0.25, 2.0} GeV^2. We take priors on the values of the spline functions at these knots. For $g_0^{0,+}$, which give the form factors in the continuum limit at physical quark masses, we take 0.75(15). This is informed by the range of the raw lattice results with pole removed (see Figure 4). The priors for the g_j, g_s and g_l are taken to be 0.0(5) and for the g_c 0.0(1.0).

The spline fit returns a χ^2/dof value of 0.66 for 65 degrees of freedom. The form factors at the physical point can then be reconstructed from the $g_0(q^2)$ spline functions along with the $(1+L(m_l))$ and pole factors. A comparison of the form factors at the physical point with those from our z-expansion fit of Section III D 1 is shown in Figure 6. We see good agreement across the q^2 range. The cubic spline results are slightly less accurate (see also Figure 5) but the cubic splines also explore non-analytic functions of q^2 that we do not expect to contribute to the form factors. This is why we prefer the z-expansion fit results.

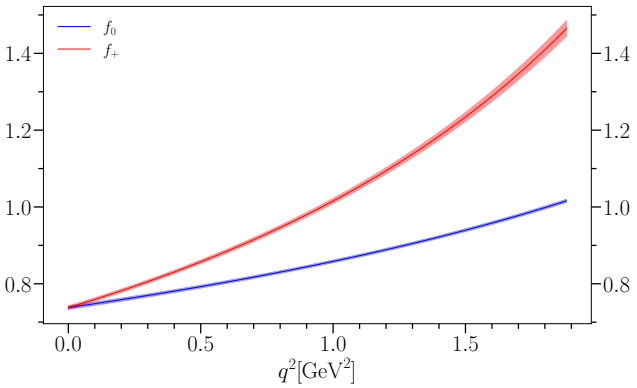

FIG. 7. Our results for the f_+ and f_0 form factors, at the physical point ($a = 0$ and physical quark masses), as a function of squared momentum-transfer, q^2.

IV. RESULTS FOR FORM FACTORS

In Section III D 1 we described how we fit the lattice form factor results, obtained at specific values of momentum for a set of lattice spacing values and quark masses, to a functional form (Eq. (24)) that allows us to interpolate in q^2 and extrapolate to zero lattice spacing and physical quark mass values. To obtain the form factor at the physical point we set $\mathcal{N}_n$ and a to zero in Eq. (26), so that $a_n^{0,+} = d_{0n}^{0,+}$. These values of a_n are then substituted into Eq. (24) with $L(m_l)$ evaluated for physical m_l/m_s (Eq. (30)) and δ_{FV} set to zero. $M_{D_s^*}$ and $M_{D^*_{s0}}$ take their experimental values [3] in the pole factors.

In our lattice calculation we have degenerate u and d quarks with mass m_l (for both valence and sea). Our physical point is defined as that where m_l has a value equal to the physical average for u and d from Eq. (30). We therefore do not distinguish between form factors for $D^0 \to K^-$ and $D^+ \to K^0$ decay. Our decay process is that for a D with the average mass of D^0 and D^+ to that of a K meson with the average mass of a K^+ and a K^0. When we determine V_{cs} in Section V we will include an uncertainty to allow for the fact that $m_u = m_d$ in our calculation.

The form factors obtained in the continuum limit and with physical quark masses are plotted as a function of q^2 in Figure 7.

Table III gives the parameters needed to reconstruct our form factors at the physical point. As discussed above these are the $a_n^{0,+}$ coefficients of the z-expansion (Eq. (23)) in the $a \to 0$ limit with physical quark masses.

TABLE III. Values and uncertainties for the fit coefficients $a_n^{0,+}$, pole masses, and chiral logarithmic term $(1 + L(m_l))$ for the reconstruction of our form factors at the physical point as a function of q^2 from Eq. (34). The correlation matrix between these parameters is given below the row with their values. The pole masses are in GeV. The pole masses and $L(m_l)$ are very slightly correlated due to the way the fit function is constructed. These correlations are too small to have any meaningful effect on the fit, but we include them for completeness in reconstructing our results.

a_0^0	a_1^0	a_2^0	a_0^+	a_1^+	a_2^+	$M_{D_s^0}^{\rm phys}$	$M_{D_s^*}^{\rm phys}$	$(1 + L(m_l))$
0.7292(43)	0.825(80)	0.72(50)	0.7292(43)	-0.95(10)	1.1(1.3)	2.31780(50)	2.11220(40)	1.01200(26)
1.00000	0.73103	0.51757	1.00000	0.29251	0.02299	-0.00023	-0.00005	-0.04904
	1.00000	0.90723	0.73103	0.49742	0.01488	-0.01619	0.00001	-0.00795
		1.00000	0.51757	0.52335	0.00600	0.00368	0.00003	-0.00222
			1.00000	0.29251	0.02299	-0.00023	-0.00005	-0.04904
				1.00000	0.49065	0.00007	-0.01488	0.00553
					1.00000	0.00019	0.00362	-0.00017
						1.00000	-0.00000	-0.00000
							1.00000	0.00000
								1.00000

The form factors are then reconstructed from

$$f_0(q^2) = \frac{(1 + L(m_l))}{(1 - q^2/M_{D_{s0}^*}^2)} \sum_{n=0}^{2} a_n^0 z^n \,,$$

$$f_+(q^2) = \frac{(1 + L(m_l))}{(1 - q^2/M_{D_s^*}^2)} \times \sum_{n=0}^{2} a_n^+ \left(z^n + \frac{n}{3}(-1)^n z^3 \right). \qquad (34)$$

Table III gives the coefficients and also their correlation matrix, including their correlations with $L(m_l)$ and the D_s^* and D_{s0}^* pole masses.

Figure 8 shows a breakdown of our errors as a function of q^2. We see that the total uncertainty is dominated by the statistical errors in the lattice QCD results. These can be reduced by collecting higher statistics, particularly on the finest lattice, set 8, where our statistical sample is not very large. The uncertainties are larger for f_+ than f_0; this is because of the way that the form factors are determined using Eqs. (10) and (11). The uncertainty for f_+ increases close to zero-recoil. This is because we have used the temporal vector current to determine f_+. Using a spatial vector current reduces this uncertainty, but it requires additional correlators to be calculated so we have not done that here. The region of q^2 close to zero-recoil is not important for the determination of V_{cs}, as we shall see in Section V A.

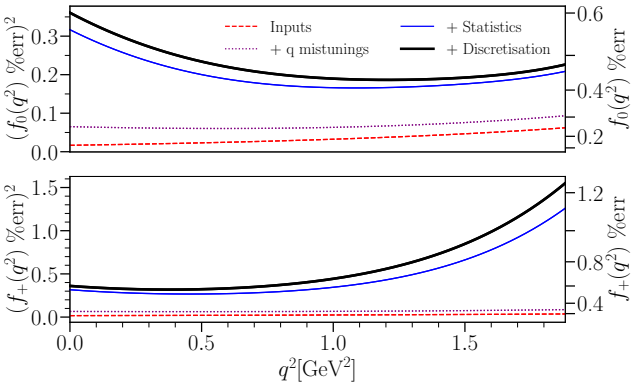

FIG. 8. Uncertainties for f_0 and f_+ (for $m_u = m_d$) as a function of q^2. The red line 'Inputs' shows the uncertainties coming from fixed inputs, such as experimental meson masses used in the analysis. The purple line 'q mistunings' adds in uncertainties arising from mistuning of valence and sea quark masses. The blue 'Statistics' line further adds the statistical uncertainties from the lattice results (correlator fits). Finally, the black line ('Discretisation') gives the total uncertainty, now including the contribution from discretisation effects. These uncertainties add in quadrature, so we plot the squared percentage error and include an axis showing the corresponding percentage error on the right for clarity.

A. Comparison to previous results

We can compare our results for the $D \to K$ form factors to those from earlier full lattice QCD calculations (all of which have $m_u = m_d$). In Figure 9 we show the comparison of results at the two ends of the physical q^2 range, $q^2 = 0$ and $q^2 = q^2_{\rm max} = (M_D - M_K)^2$. For our results at $q^2_{\rm max}$ we use, as discussed above, $M_D = (M_{D^+} + M_{D^0})/2$ and $M_K = (M_{K^+} + M_{K^0})/2$. Previous results are from HPQCD: [19] calculating only the scalar form factor (in order to obtain the vector form factor at $q^2 = 0$ from $f_+(0) = f_0(0)$) and [20] calculating the vector and scalar form factors across the full q^2 range of the decay. Both of these calculations were done on gluon field configurations that include 2+1 flavours of asqtad sea quarks. More recently ETMC has completed a calculation of the vector and scalar form factors across the full q^2 range

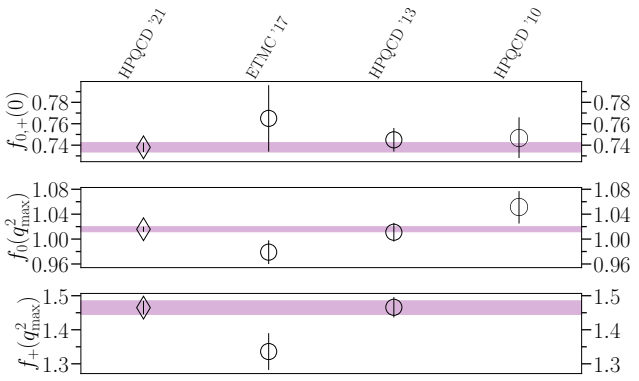

FIG. 9. Comparison of our lattice form factors at $q^2 = 0$ and $q^2_{\rm max}$ with earlier lattice QCD calculations. The points marked 'HPQCD '10' are from [19]; the points marked 'HPQCD '13' from [20] and the points marked 'ETMC '17' from [21, 22]. A preliminary analysis of the scalar form factor in [24] gives $f_0(0) = 0.768(16)$, but we have not plotted that point. Our new results (Eq. (35)) are labelled 'HPQCD '21' and demonstrate a significant improvement in uncertainty over earlier values.

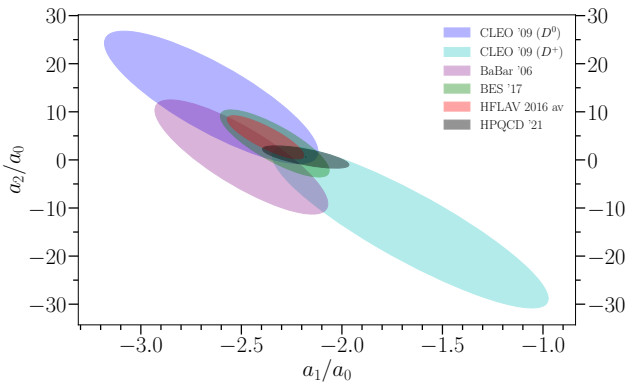

FIG. 10. Comparison of the shape of the vector form factor for $D \to K$ expressed in terms of ratios of the z-expansion coefficients a_1 and a_2 to a_0 for the fit form of Eq. (36). Ellipses give the 68% confidence limits ($\Delta\chi^2 = 2.3$). Experimental results are from [50–53]. CLEO results are for $D^0 \to K^- e^+ \nu_e$ (dark blue) and $D^+ \to \bar{K}^0 e^+ \nu_e$ (light blue); all other experimental data is for $D^0 \to K^- e^+ \nu_e$. The HFLAV experimental average [53] is given as the red ellipse. Our results here are given by the black ellipse, showing good agreement.

using gluon field configurations with 2+1+1 flavours of twisted-mass sea quarks [21, 22]. Our results here include 2+1+1 flavours of HISQ sea quarks and are plotted as the leftmost results in Figure 9. They show a significant improvement in uncertainty over the earlier results.

Our results (plotted in Figure 9) are

$$\begin{aligned} f_{+,0}(0) &= 0.7380(44)\,, \\ f_0(q^2_{\rm max}) &= 1.0158(41)\,, \\ f_+(q^2_{\rm max}) &= 1.465(20)\,. \end{aligned} \tag{35}$$

We observe a 2σ tension with the results of [21] at $q^2_{\rm max}$.

Since the experimental differential rate for light leptons is proportional to the square of the vector form factor (Eq. (8)), the form factor shape can be determined from experiment. The experimental shape parameters come from a z-expansion fit but from a somewhat different one to the one that we have used here. To make a comparison we therefore need to fit our results in terms of the z-expansion used by the experiments. We do this by a 'refitting' procedure that we describe in Appendix B. The fit form used by the experiments is [40]

$$f_+(q^2) = \frac{1}{z(q^2, t_0 = M^2_{D_s^*})\phi(q^2)} \sum_{n=0}^{N-1} a_n z^n, \tag{36}$$

where ϕ is an 'outer function' given in Eq. (B2) and t_0 is taken to be the value which minimises the maximum value of z in the q^2 to z mapping (Eq. (23)). The ratios a_1/a_0 and a_2/a_0 and their correlation coefficient then define the shape of the vector form factor. Experimental results from [50–52] are plotted in Figure 10.

By fitting our form factors at the physical point (from Table III) to the form in Eq. (36) we obtain $a_1/a_0 = -2.18(14)$ and $a_2/a_0 = 0.6(1.5)$ with a correlation coefficient of $\rho_{12} = -0.70$. As is clear from Figure 10 this agrees well with the experimental shape parameters, providing a good test of QCD. The HFLAV average [53] of the shape parameters is more accurate than the individual experimental results giving $a_1/a_0 = -2.38(13)$; $a_2/a_0 = 4.7(3.0)$ and $\rho_{12} = -0.19$. The agreement of our results with this average is particularly striking.

B. Tests of lepton flavour universality

In the Standard Model the three charged leptons are copies of each other apart from having different masses. Hints are seen in experiment of violations of this lepton flavour universality in B decays (for a review see [54]) and this motivates a search for this also in D decays [55, 56]. We can only compare results with μ and e in the final state for $D \to K$ decay because the production of τ leptons is kinematically forbidden. The BES experiment recently measured the ratio $R_{\mu/e}$ of branching fractions to μ and to e as a function of q^2 [57]. We can calculate this ratio very accurately from our form factor results using Eq. (8), because there is a lot of cancellation of uncertainties in the form factors in the ratio. If we ignore long-distance QED corrections (to be discussed below) we can compare the BES results to the curve derived from our form factors (solid black line) in Figure 11. We see good agreement across the q^2 range. To quantify this agreement it would be necessary to have a correlation matrix for the experimental results. $R_{\mu/e}$ is smaller than 1 at small values of q^2, where the factor $(1-\epsilon)^2$ in Eq. (8) has an effect for the μ. It is larger than 1 at large values

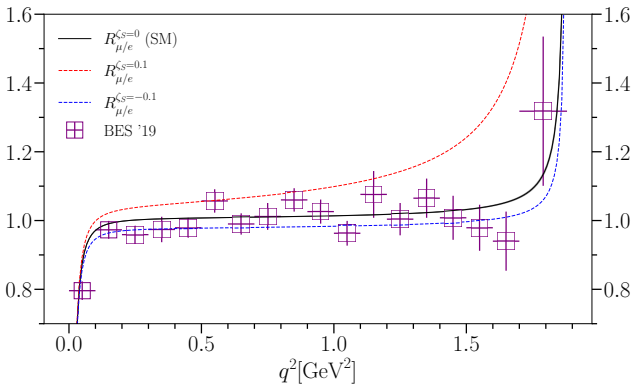

FIG. 11. Lepton flavour universality tests in $D \to K$ decay. The solid black curve as a function of q^2 shows the Standard Model ratio of branching fractions for a muon in the final state to that for an electron obtained from our form factors using Eq. (8). The width of the curve gives the (very small) uncertainty from our results. Possible QED effects are not included here. The points, with error bars, are from the BES experiment [57]. For illustration the red and blue dashed lines show what the curve would look like in the presence of a new physics scalar coupling for the μ case (see Eq. (38) for definition of ζ_S).

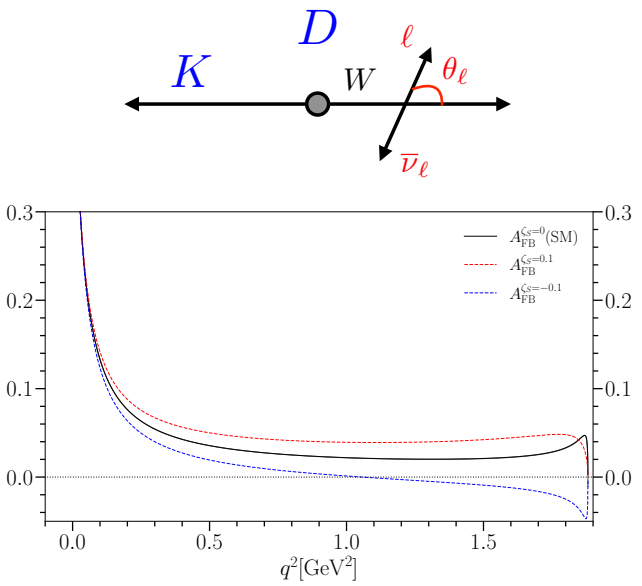

FIG. 12. The forward-backward asymmetry of the muon produced in $D \to K$ decay. This is defined with respect to the angle θ_ℓ in the W rest-frame indicated in the figure at the top. The solid black line shows the Standard Model result derived from our form factors, including the lattice QCD uncertainty but ignoring any uncertainty from possible QED corrections. For illustration the red and blue dashed lines show what the curve would look like in the presence of a new physics scalar coupling for the μ case (see text and Eq. (38)).

of q^2 where the term containing the scalar form factor, f_0, contributes.

The ratio of branching fractions to μ and to e, $R_{\mu/e}$, can be obtained by integrating Eq. (8) from $q^2 = m_\ell^2$ to $q^2_{\rm max}$. We take $q^2_{\rm max}$ from the D and K masses averaged over charged and neutral cases, although other choices make negligible difference. Our result for the ratio of branching fractions then has a 0.02% uncertainty from lattice QCD. A larger source of uncertainty is the difference of long-distance QED corrections to the rate in the μ and e cases. This could be a sizeable effect when there are electrically charged mesons in the final state, as in the BES experimental results which correspond to $D^0 \to K^-$ decay. Our result for $R_{\mu/e}$ is then

$$R_{\mu/e} = 0.9779(2)_{\rm latt}(50)_{\rm EM}, \tag{37}$$

allowing a 0.5% uncertainty for the difference of QED corrections in the $D^0 \to K^-$ case. Our $R_{\mu/e}$ agrees well with the BES result of 0.974(7)(12) [57] but is much more accurate. We see some tension with the earlier ETMC result [22] for this ratio using lattice QCD of $0.975(1)_{\rm latt}$.

Violation of lepton flavour universality might be seen in comparison to the curve of Figure 11 with accurate enough experimental results, up to possible QED effects. We illustrate the impact of a new physics scalar coupling in the μ sector, $C_S^{(\mu)}$, with red and blue dashed lines. $C_S^{(\mu)}$ would multiply a new physics contribution to the effective Lagrangian consisting of a scalar $\overline{s}c$ current multiplying a $\overline{\nu}_\mu\mu$ current. Such a term affects the $D \to K$ differential rate, modifying the coefficient of the scalar form factor in Eq. (8) by a factor of $|(1 + C_S^{(\mu)} q^2/(m_\mu(m_s - m_c)))|^2$ [55] where m_s and m_c are the strange and charm quark masses. We show results for two possible real values of C_S such that

$$\zeta_S \equiv \frac{C_S^{(\mu)}}{m_s - m_c} = \pm 0.1\,{\rm GeV}^{-1}, \tag{38}$$

which roughly encompass the range of variation of the central values of the BES data points from our Standard Model curve.

Angular variables can also provide sensitive tests of the Standard Model and constraints on new physics. Figure 12 plots the forward-backward asymmetry, A_{FB}, of the muon in $D \to K\mu\overline{\nu}$ decay as a function of q^2 in the Standard Model from our form factors (solid black line), ignoring possible QED corrections. This asymmetry is defined using the angle θ_ℓ between the charged lepton momentum in the W rest-frame and the W momentum vector in the D rest-frame. θ_ℓ is shown in Figure 12 and takes the range 0 to π. A_{FB} is then defined as

$$A_{FB}^{(\ell)}(q^2) = -\frac{b_\ell}{d\Gamma^{(\ell)}/dq^2} \tag{39}$$

where

$$\frac{d\Gamma^{(\ell)}}{dq^2 d\cos\theta_\ell} = a_\ell(q^2) + b_\ell(q^2)\cos\theta_\ell + c_\ell(q^2)\cos^2\theta_\ell. \tag{40}$$

$A_{FB} = 0$ for massless leptons because only the helicity zero component of the W can contribute. For massive leptons there is an interference term between scalar and vector form factor contributions [55]. Figure 12 shows that this has a sizeable effect for muons in the final state, particularly close to $q^2 = 0$.

$A_{FB}^{(\mu)}$ for $D \to K$ decay would be modified in the presence of a (real) scalar coupling from new physics because this affects the vector/scalar interference term. Figure 12 shows the impact of two possible values of this coupling, as in Eq. (38) and Figure 11. The impact of the new coupling is mainly at large q^2 values where A_{FB} is small. A positive value of $C_S^{(\mu)}$ (negative value of ζ_S) can change the sign of A_{FB} from that expected in the Standard Model at large q^2.

V. DETERMINATION OF $|V_{cs}|$

Using the measured experimental rates for the $D \to K\ell\overline{\nu}$ decay we can determine the CKM element $|V_{cs}|$. The accuracy with which this can be done depends on the accuracy of both the experimental results and the accuracy of the lattice QCD form factors for the decay process. We show here that our improved form factor determination yields a significant improvement in the values of V_{cs} obtained. We give three different methods for determining V_{cs}. Our preferred approach (Section V A) is to use the experimental differential decay rate and Eq. (8), integrated over the q^2 bins used by the experiment [20]. This is the most direct approach, enabling use of the q^2 region where the experimental results are most accurate and testing the q^2-dependence of the differential rate at the same time (although agreement here has already been demonstrated in Figure 10). It requires experimental measurement of the differential rate with a covariance matrix for results in different bins and this is not always possible. We therefore also determine V_{cs} in Section V B from the total rate, integrated over all q^2. In Section V C we apply a third method that uses quoted experimental values from fitting the differential rate and extrapolating to $q^2 = 0$.

Before giving details of these methods, we first discuss and estimate two further sources of systematic uncertainty beyond those of our calculated form factors and the experimental results:

1. $m_u \neq m_d$. In determining V_{cs} we will use our form factors obtained in QCD with $m_u = m_d$. The experimental results, however, correspond to the case with either valence u quarks (for D^0 decay) or valence d quarks (for D^+ decay). We therefore need to allow an uncertainty in our calculation for this mismatch. In determining the form factors at the physical point in Section III D we set the physical value of the light quark mass, m_l, from Eq. (30). We can test the effect of having a different light quark mass (corresponding to u or d) by changing this condition. We take $m_d/m_u \approx 2$ [3] so that $m_u/m_s \approx 2/(3 \times 27.18)$ and $m_d/m_s \approx 4/(3 \times 27.18)$ and compare to our original results using Eq. (30). We find a change in our form factors of, at most, 0.15%. Note that the calculation we really want to match to experiment changes only the light valence quark mass to u or d, leaving the sea the same (with u and d quarks that match, to a linear approximation in quark mass, two quarks with mass m_l equal to their average). To do this would require additional lattice calculations so here we simply take an additional uncertainty of 0.15% on our form factors (across the q^2 range) to account for this. This corresponds to 0.25σ at $q^2 = 0$ (see Eq. (35)).

2. *QED.* Another issue that we must address in determining V_{cs} is that of (long-distance) electromagnetic corrections. There are QED effects inside the mesons arising (mainly) from the valence quark electric charges. There are also effects from photon radiation, mainly from final-state interactions, that could be more sizeable for the case where a charged K is produced. The experimental results include tests and corrections for radiated photons, to produce a photon-inclusive rate; this is typically done using PHOTOS [58] (see, for example, the discussions in [50, 51]). In Eq. (8) we include a factor of $(1 + \delta_{EM})$ to allow for the effects of QED radiation as a q^2-independent uncertainty, since these effects have not been calculated. For $K \to \pi$ semileptonic decay, where the electromagnetic corrections have been calculated, results range from $\delta_{EM} \approx 0$ for neutral final state mesons to $\delta_{EM} \approx 0.7\%$ [59] for charged final state mesons and with small differences between e and μ leptons in the final state. Here we will take independent uncertainties of $\delta_{EM} = \pm 1\%$ for the charged final state case ($D^0 \to K^+$) and $\pm 0.5\%$ for the neutral final state case ($D^+ \to K^0$). We will also take independent δ_{EM} for the case with final state μ from that with final state e, since these could differ. In our final result we will keep the QED uncertainty as a separate factor so that in the future it can be adjusted in the light of new information on these corrections (for example from lattice QCD+QED calculations [60]).

A. Using the differential rate

We can use our form factor results across the full physical q^2 range to compare bin by bin in q^2 with experimental values of partial decay rates. For a given bin (q_i^2, q_{i+1}^2) the partial width is given by (from Eq. (8))

$$\begin{aligned}\Delta_i\Gamma &= \int_{q_i^2}^{q_{i+1}^2} \frac{d\Gamma}{dq^2} dq^2 \qquad (41)\\ &= \frac{G_F^2 |\eta_{EW} V_{cs}|^2 (1+\delta_{EM})}{24\pi^3} \times \\ &\int_{q_i^2}^{q_{i+1}^2} dq^2 \left[|\vec{p}_K|^3 (1-\epsilon)^2 (1+\frac{\epsilon}{2}) |f_+(q^2)|^2 \right. \\ &\left. + |\vec{p}_K| (1-\epsilon)^2 M_D^2 \left(1 - \frac{M_K^2}{M_D^2}\right)^2 \frac{3\epsilon}{8} |f_0(q^2)|^2 \right].\end{aligned}$$

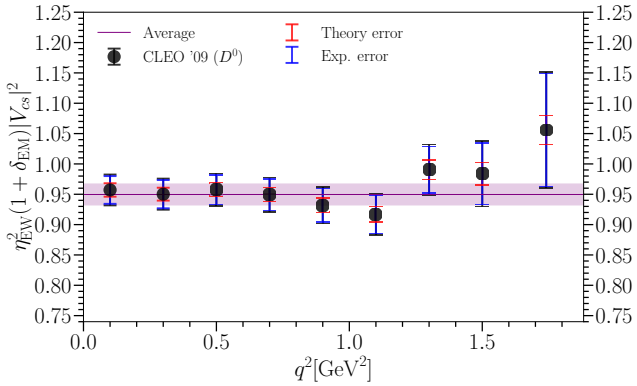

FIG. 13. Plot of the determination of $|\eta_{EW}V_{cs}|^2(1+\delta_{EM})$ per q^2 bin for CLEO D^0 results [50]. The total uncertainty for each bin is given in black and this is broken down into experimental (blue) and theoretical (red) contributions, the latter coming from our form factors. Each data point is centred on the q^2 bin it corresponds to. Note that the uncertainties are correlated between q^2 bins. The purple band gives the weighted average for these data points, with all correlations included.

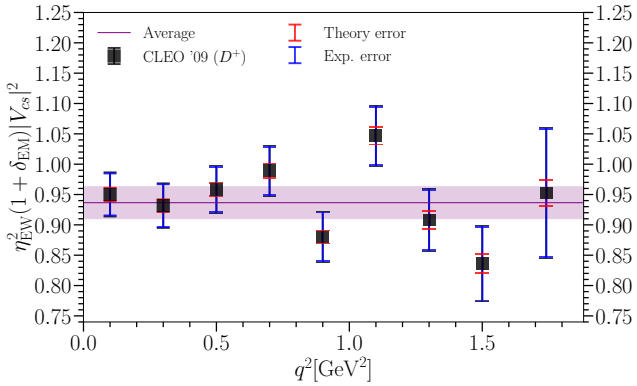

FIG. 14. Plot of the determination of $|\eta_{EW}V_{cs}|^2(1+\delta_{EM})$ per q^2 bin for CLEO D^+ results [50]. The total uncertainty for each bin is given in black and this is broken down into experimental (blue) and theoretical (red) contributions, the latter coming from our form factors. Each data point is centred on the q^2 bin it corresponds to. Note that the uncertainties are correlated between q^2 bins. The purple band gives the weighted average for these data points, with all correlations included.

The terms containing $\epsilon \equiv m_\ell^2/q^2$ have almost no impact here for either $\ell = e$ or $\ell = \mu$ but we include them nevertheless. We take $G_F = 1.1663787(6) \times 10^{-5}\text{GeV}^{-2}$ [3] from the muon lifetime and $\eta_{EW} = 1.009(2)$ (Eq. (9)). $(1 + \delta_{EM})$ allows for uncertainty from electromagnetic corrections, as discussed above. We perform the integral on the right-hand side of Eq. (41) numerically for each $\Delta_i\Gamma$ matching those used in the experiment and carefully including the correlations of the form factor values between bins. As discussed above we use our form factors

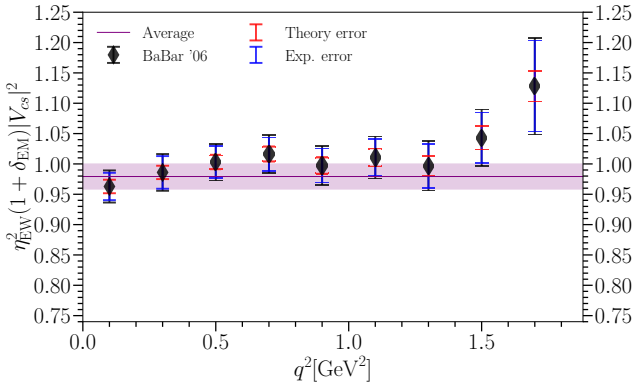

FIG. 15. Plot of the determination of $|\eta_{EW}V_{cs}|^2(1+\delta_{EM})$ per q^2 bin for BaBar D^0 results [51]. The total uncertainty for each bin is given in black and this is broken down into experimental (blue) and theoretical (red) contributions, the latter coming from our form factors. Each data point is centred on the q^2 bin it corresponds to. Note that the uncertainties are correlated between q^2 bins. The purple band gives the weighted average for these data points, with all correlations included.

determined using $m_u = m_d$ and include an additional 0.15% uncertainty to allow for variations between this and the experimental cases. For all of the kinematic factors in Eq. (41) we use the experimental meson masses [3] for the charged or neutral meson cases as appropriate for that set of experimental data.

Comparison to the experimental results enables us to determine $|\eta_{EW}V_{cs}|^2(1+\delta_{EM})$ for each bin and obtain a result as a weighted average across q^2 bins. We use experimental results for which a covariance matrix is provided for the partial rates between q^2 bins. We add covariance matrices for statistical and systematic uncertainties where they are provided separately (effectively adding the uncertainties in quadrature). In some cases an overall uncertainty on each bin is given along with the percentage breakdown into systematic and statistical uncertainty. We use this, along with the correlation matrices given, to obtain the separate covariance matrices and add them.

CLEO results are taken from [50], where both $D^0 \to K^- e^+ \nu_e$ and $D^+ \to \overline{K}^0 e^+ \nu_e$ differential rates are measured and the correlations between them given. Partial rates were taken from Table V, and σ_i^{stat}, σ_i^{syst} and their covariance matrices were calculated using these, the percentage error breakdowns in Tables VII and VIII and the correlation matrices in Tables XVI and XVII. These covariance matrices are then easily included in our calculation using the gvar package [37]. Our determination of V_{cs} on a bin-by-bin basis is shown for the CLEO results in Figures 13 and 14. The fit for the weighted average gives a χ^2/dof of 0.64 in the D^0 case and 1.7 in the D^+ case. In both cases there are nine degrees of freedom. The q^2 bins with the minimum total uncertainty are at the small q^2 end of the range, where the experiment is

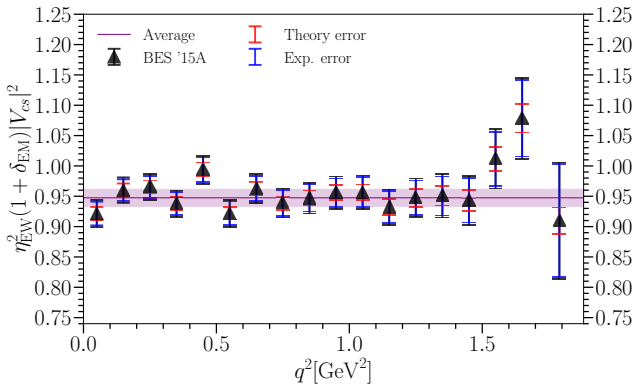

FIG. 16. Plot of the determination of $|\eta_{EW}V_{cs}|^2(1+\delta_{EM})$ per q^2 bin for BES D^0 results [52]. The total uncertainty for each bin is given in black and this is broken down into experimental (blue) and theoretical (red) contributions, the latter coming from our form factors. Each data point is centred on the q^2 bin it corresponds to. Note that the uncertainties are correlated between q^2 bins. The purple band gives the weighted average for these data points, with all correlations included.

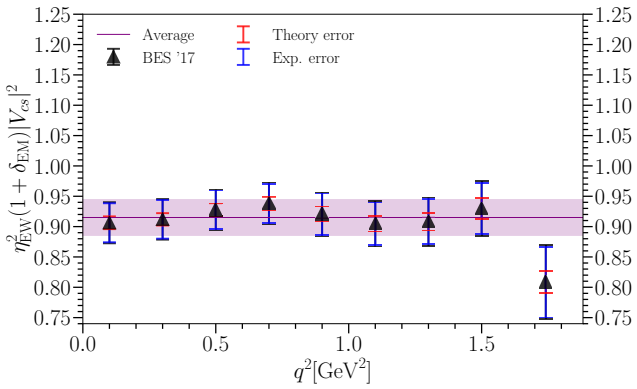

FIG. 17. Plot of the determination of $|\eta_{EW}V_{cs}|^2(1+\delta_{EM})$ per q^2 bin for BES D^+ results [61]. The total uncertainty for each bin is given in black and this is broken down into experimental (blue) and theoretical (red) contributions, the latter coming from our form factors. Each data point is centred on the q^2 bin it corresponds to. Note that the uncertainties are correlated between q^2 bins. The purple band gives the weighted average for these data points, with all correlations included.

most accurate.

BaBar results are taken from [51]; these are for the $D^0 \to K^- e^+ \overline{\nu}_e$ decay normalised by the branching fraction for $D^0 \to K^-\pi^+$. Table II gives the normalised decay distribution and total correlation matrix. The leading diagonal values of the matrix give the σ_i. The distribution has been normalised so that the sum over all bins equals unity. A value is also given for

$$R = \frac{\mathcal{B}(D^0 \to K^- e^+ \nu_e)}{\mathcal{B}(D^0 \to K^-\pi^+)}, \tag{42}$$

which is included in the correlation matrix. Using this value, and multiplying by the global average for $\mathcal{B}(D^0 \to K^-\pi^+) = 0.03950(31)$ [3], we determine $\mathcal{B}(D^0 \to K^- e^+ \nu_e)$. This allows us to extract the branching fractions per bin from the decay distribution and convert these to partial rates by dividing by the D^0 lifetime $\tau_{D^0} = 4.101(15) \times 10^{-4}$ ns [3]. We drop the largest q^2 bin from our weighted average fit (because it is equal to one minus the sum of the others from the normalisation constraint). We include the normalisation uncertainty after averaging to avoid normalisation bias. Our determination of V_{cs} from the BaBar results is shown in Figure 15 and has a χ^2/dof of 0.9 with nine degrees of freedom.

BES results are taken from [52] for the D^0 decay channel. The data can be found in Table V, and the breakdown of the percentage errors and correlation matrices for systematic and statistical uncertainty are given in Tables IX and XI. BES results for the D^+ channel are given in [61] (Table VI). Our determination of V_{cs} on a bin-by-bin basis is shown for these two sets of BES results in Figures 16 and 17, with χ^2/dof 1.1 (dof = 18) and 0.9 (dof = 9) respectively.

The determinations of V_{cs} from each experiment and each q^2 bin are plotted together as a function of q^2 in Figure 18. The weighted averaged results for $|V_{cs}|$ for each experiment are then compared in Figure 19. The $|V_{cs}|$ result for each experiment is obtained by dividing the square root of the weighted average of $|V_{cs}|^2\eta_{EW}^2(1+\delta_{EM})$ over the q^2 bins by $\eta_{EW}\sqrt{(1+\delta_{EM})}$.

The results from each experiment are combined to give a total average for $|V_{cs}|$ which is shown by the purple band in Figures 18 and 19. Here we have assumed that correlations between the different experiments can be ignored. However, we do not include both sets of BES data, since the correlations between the two sets are not given. We include the more precise BES D^0 results [52] in Figure 18 and drop the BES D^+ values. We note that in each q^2 bin the experimental error dominates over that from theory (our form factors). The fact that there are multiple sets of uncorrelated experimental results but only one set of lattice QCD form factors means that in the final average, however, the theory uncertainty dominates. We obtain a value of

$$|V_{cs}|^{\mathrm{d}\Gamma/\mathrm{d}q^2} = 0.9663(53)_{\mathrm{latt}}(39)_{\mathrm{exp}}(19)_{\eta_{EW}}(40)_{\mathrm{EM}} \tag{43}$$

from using the binned differential rate. The fit to yield the average has a χ^2/dof of 0.7 for 4 degrees of freedom. The first uncertainty here is from our lattice QCD form factors, including an uncertainty for the fact that these are calculated for the $m_u = m_d$ case. The second uncertainty comes from the experimental results. The third uncertainty is from η_{EW} and the fourth from long-distance QED corrections, amounting to 0.5% in V_{cs} for the case of a charged meson in the final state, and 0.25% for a neutral meson in the final state, as discussed above. There is some sign in Figures 18 and 19 that the central values of V_{cs} for the results with a charged K^- meson in the final state are slightly higher than those with a

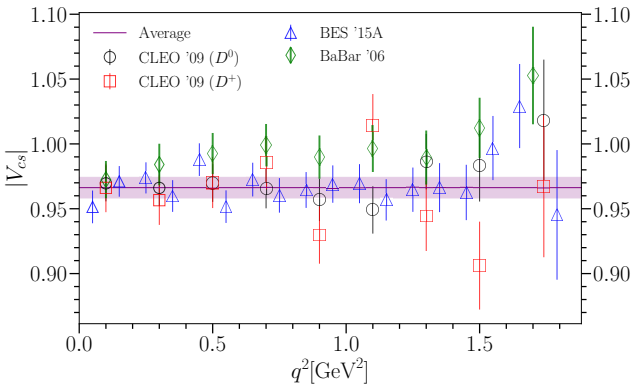

FIG. 18. Plot of $|V_{cs}|$ per bin for CLEO, BaBar and BES results from [50–52]. Each data point is centred on the q^2 bin it corresponds to and the error bars plotted include the uncertainties from η_{EW} and δ_{EM}. The purple line and band give the result from our total weighted average for $|V_{cs}|^2$, with all correlations included. The width of the band includes the uncertainties from η_{EW} and δ_{EM} as given in Eq. (43).

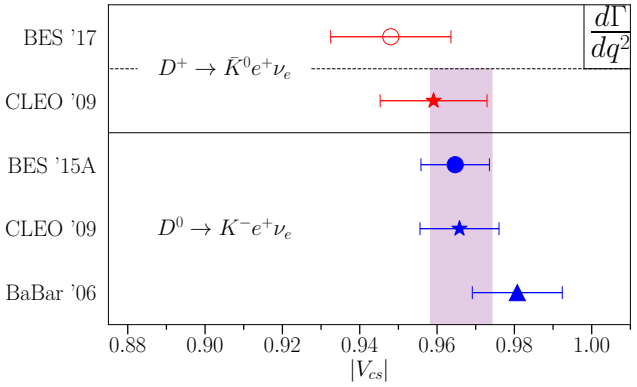

FIG. 19. Comparison plot of the determinination of $|V_{cs}|$ using the differential decay rate for CLEO, BaBar and BES results from [50–52, 61] for D^0 and D^+ decays. The purple band gives the total weighted average for V_{cs}, not including the BES '17 result. The width of the band includes the uncertainties from η_{EW} and δ_{EM} as given in Eq. (43).

neutral $\overline{K}^0$ meson; this is consistent with what might be expected from QED effects if $\delta_{EM} > 0$ but the uncertainties are too large for this to be clear. The fit to the average uses this information to arrive at the combined uncertainty from EM effects above.

B. Using the total branching fraction

We can also determine V_{cs} from a comparison of theory and experiment for the total branching fraction for the semileptonic decay process. To obtain the total width, Γ, from the theory side we need to integrate Eq. (8) over the full physical q^2 range. The limits of integration use the experimental masses for the appropriate leptons and charged or neutral meson masses. Table IV gives our values for $\Gamma/(|\eta_{EW}V_{cs}|^2(1+\delta_{EM}))$ for each of the 4 modes we consider, i.e. charged and neutral D meson decay to e and μ in the final state.

TABLE IV. Total width for $D \to K$ semileptonic decay up to a factor of $|\eta_{EW}V_{cs}|^2(1+\delta_{EM})$ (see Eq. (8)), determined from our form factors. We give results for all 4 modes that we consider. They differ slightly in the parent and daughter meson masses and in the mass of the lepton in the final state; these affect the kinematic factors in the differential rate and the end-points of integration for the total width. These values can be combined with experimental values of the relevant branching fraction and D meson lifetime to determine $|V_{cs}|$.

	$\Gamma/(\lvert\eta_{EW}V_{cs}\rvert^2(1+\delta_{EM}))$ (ns^{-1})
$D^+ \to \overline{K}^0 \mu^+ \nu_\mu$	88.30(99)
$D^+ \to \overline{K}^0 e^+ \nu_e$	90.3(1.0)
$D^0 \to K^- \mu^+ \nu_\mu$	87.57(98)
$D^0 \to K^- e^+ \nu_e$	89.5(1.0)

We convert the total width to a branching fraction using the experimental average values for the appropriate D meson lifetime [3]. Comparison to experiment then yields a determination of $|V_{cs}|$. There are additional experimental results for the total branching fraction beyond those used in the determination of $|V_{cs}|$ from the differential decay rate in Section V A. These come from Belle [62] for D^0 decays to both e and μ in the final state and from BES for D^0 decays to μ in the final state [57] (discussed in Section IV B in the context of tests of lepton flavour universality) and D^+ decays to μ in the final state [63]. There are also new results from BES [64] for D^0 and D^+ decay to e in the final state, using a new reconstruction method. In the summary of [64] total branching fractions are quoted that are the average of the new results with their earlier values [52, 61], accounting for correlations. It is these averages that we use in the following, denoting them as 'BES21'. Note that there are then branching fraction results for all four possible modes for $D \to K$ decay.

Figure 20 shows the results of the determination of V_{cs} using the total branching fraction for each experimental result. In fitting the experimental results to give a common (average) $|V_{cs}|$ value we have taken the systematic uncertainties for a given experiment to be 100% correlated between the different results from that experiment. We obtain a final result for V_{cs} from the total branching fraction of

$$|V_{cs}|^{\mathcal{B}} = 0.9686(54)_{\rm latt}(39)_{\rm exp}(19)_{\eta_{EW}}(30)_{\rm EM}. \qquad (44)$$

This fit has a χ^2/dof of 1.7 for 9 degrees of freedom. Again the first uncertainty here is from our form factors (including an uncertainty from $m_u \neq m_d$), the second from the experimental results (including uncertainties from the D meson lifetime), the third from η_{EW} and

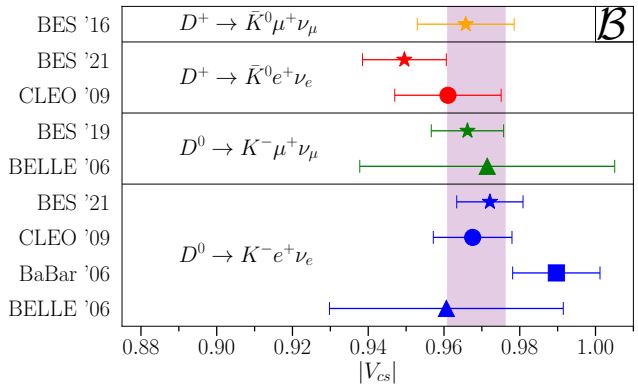

FIG. 20. Comparison plot of the determination of $|V_{cs}|$ using the total branching fraction. Experimental results are from [63] for $D^+ \to \overline{K}^0\mu^+\nu_\mu$, [50, 64] for $D^+ \to \overline{K}^0 e^+\nu_e$, from [57, 62] for $D^0 \to K^-\mu^+\nu_\mu$ and from [50, 51, 62, 64] for $D^0 \to K^- e^+\nu_e$ decays. Note that the BES results for final state e are the quoted averages for results from [64] and [52, 61]. The purple band gives the total average for V_{cs}, assuming 100% correlation of systematic uncertainties for results from a given experiment. The width of the purple band encompasses all uncertainties, including those from η_{EW} and δ_{EM}.

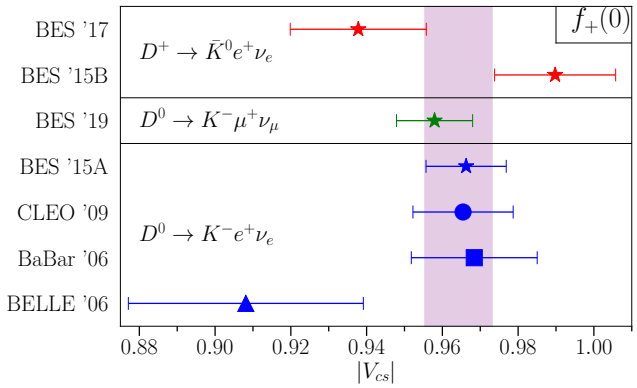

FIG. 21. Comparison plot of the determination of $|V_{cs}|$ using the extrapolation of experimental results to $q^2 = 0$. Experimental results are from [61, 65] for $D^+ \to \overline{K}^0 e^+\nu_e$, from [57] for $D^0 \to K^-\mu^+\nu_\mu$ and [50–52, 62] for $D^0 \to K^- e^+\nu_e$. The purple band gives the weighted average result for V_{cs} obtained from the HFLAV weighted average [10] of the experimental results but including a correction for η_{EW} and an additional uncertainty from QED corrections (Eq. (45)).

the fourth is the uncertainty we allow for QED corrections from δ_{EM}. δ_{EM} is taken as an independent uncertainty for the e and μ cases and for charged and neutral mesons and the fit for the average constrains this uncertainty based on the data. The χ^2/dof value drops to 1.4 if the BaBar result for $D^0 \to K^-$ is omitted from the fit; the average value obtained then falls by 0.35σ (where σ is the total uncertainty).

C. Using $f_+(0)$

Following the approach for K semileptonic decays, experimental groups have often provided results for the combination of $|V_{cs}|$ and form factor values at $q^2 = 0$ derived from fitting their differential decay rates. Simply dividing these results by the lattice QCD form factor result at $q^2 = 0$ can then give a determination of V_{cs}. However, what is generally quoted as a value for $|V_{cs}|f_+(0)$ is, in our notation using Eq. (8), in fact $|V_{cs}|f_+(0)\eta_{EW}\sqrt{(1+\delta_{EM})}$. Taking this into account, and using our $f_+(0)$ result from Eq. (35), gives results for V_{cs} from the experimental results available that are plotted in Figure 21.

To determine a weighted average for V_{cs} from these values we take the HFLAV average [10] for $|V_{cs}|f_+(0)\eta_{EW}\sqrt{(1+\delta_{EM})}$ (denoted $|V_{cs}|f_+(0)$ in [10] and given as 0.7180(33)). This gives the purple band in Figure 21. The value of V_{cs} from this approach is then

$$|V_{cs}|^{f_+(0)} = 0.9643(57)_{\rm latt}(44)_{\rm exp}(19)_{\eta_{EW}}(48)_{\rm EM}. \quad (45)$$

Again the last two uncertainties come from the uncertainty on η_{EW} and QED corrections included in δ_{EM}. Since the HFLAV average includes charged and neutral meson results and μ and e final states, we take the largest uncertainty for δ_{EM} that we use here (1% in the rate) and add this as a separate uncertainty.

VI. DISCUSSION: V_{cs}

We have determined $|V_{cs}|$ in three different ways, with results given in Eqs. (43), (44) and (45). The results vary in the experimental results that are included and the way in which the lattice QCD form factors enter the calculation. The agreement between the results is good, with the lowest ($V_{cs}^{f_+(0)}$) and highest ($V_{cs}^{\mathcal{B}}$) differing by 0.6σ. This is a good test, at this level of precision, that QCD gives the shape of the form factors seen in experiment (backing up Figure 10). The uncertainties in each value are very similar, ranging from 0.8% in both our preferred approach of $V_{cs}^{{\rm d}\Gamma/{\rm d}q^2}$ and for $V_{cs}^{\mathcal{B}}$ to 0.9% for $V_{cs}^{f_+(0)}$. This high accuracy is achievable because of good statistical precision over a range of lattice spacing values and light quark masses, with accurately tuned c and s masses and weak current operators that are normalised fully nonperturbatively within the same calculation.

Figure 22 compares our new results for V_{cs} to those from earlier full lattice QCD calculations. These go back to the Fermilab/MILC result of 2004 [18], completed before experimental results were available, using the clover action for c quarks on gluon field configurations with $N_f = 2+1$ flavours of asqtad sea quarks. The HPQCD results from 2010 [19] and 2013 [20] use the HISQ action on the same gluon field configurations; we build on these

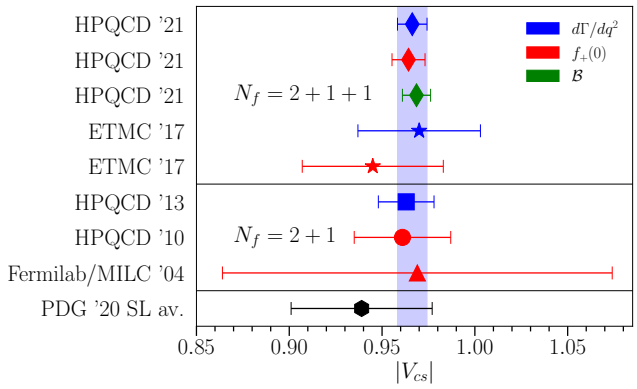

FIG. 22. Our $|V_{cs}|$ result compared with other $N_f = 2+1+1$ and $N_f = 2+1$ results using lattice QCD. Different symbols indicate different lattice calculations, whilst different colours indicate the method used. Blue indicates use of the differential rate in q^2 bins, red indicates use of the $f_+(0)$ method and green indicates use of the total branching fraction for the decay. Points marked 'HPQCD '21' come from this work, 'ETMC '17' is from [21, 22], 'HPQCD '13' is from [20], 'HPQCD '10' is from [19] and 'Fermilab/MILC '04' is from [18]. For comparison we give at the bottom the value currently quoted in the Particle Data Tables [3] from semileptonic $D \to K$ decay (Eq. (6)). The blue band carries our preferred result, $V_{cs}^{\mathrm{d}\Gamma/\mathrm{d}q^2}$, down the plot.

calculations with the improvements we have made here. The 2017 ETMC results [21, 22] use the twisted mass formalism on gluon field configurations with $N_f = 2+1+1$ flavours of sea quarks. We see good agreement between the results, including between those with $N_f = 2+1$ and $N_f = 2+1+1$ flavours.

Our results show a significant improvement in uncertainty compared to these earlier values, being a factor of two more accurate than the previous best result from HPQCD in 2013. We note that the previous results set η_{EW} to 1 and did not include an uncertainty to allow for long-distance QED effects on the experimental results.

Our preferred result for V_{cs} is

$$V_{cs} = 0.9663(80), \tag{46}$$

from Eq. (43), adding uncertainties in quadrature. We can compare this to the result for V_{ud} of 0.97370(14) from [3]. We see that $V_{cs} = V_{ud}$ within the 1σ uncertainty in Eq. (46), in good agreement with the expectation from the CKM matrix that this should be true up to effects of order $\lambda^4 \approx 0.002$.

We now compare our new result for V_{cs} from semileptonic $D \to K$ decay to the value obtained from D_s leptonic decay and look at the impact that our improved uncertainty has on our understanding of the unitarity of the CKM matrix.

Figure 23 plots the $\pm 1\sigma$ band for our determination of V_{cs} from Eq. (46) as the darker blue band. This is compared to the result (red band) from D_s leptonic decay of 0.983(18) from the 'Leptonic decays of charged pseudoscalar mesons' review in [3]. This result uses lattice QCD results for the D_s decay constant and includes uncertainties for η_{EW} and long-distance QED effects. The 'CKM Quark-Mixing Matrix' review gives a value of 0.992(12) but without including these effects. This value would then lie in the upper half of the V_{cs} leptonic band plotted in Figure 23. In either case it is clear that our new result for V_{cs} is more accurate than that from leptonic decay and has a lower central value.

Figure 23 also shows the constraints currently available on V_{cd}. The 'CKM Quark-Mixing Matrix' review in [3] quotes a value for V_{cd} from semileptonic $D \to \pi$ decay from combining experimental results with the form factor at $q^2 = 0$ determined in $N_f = 2+1+1$ lattice QCD by ETMC [21]. This gives $V_{cd} = 0.2330(136)$. The value quoted in the same review from D^+ leptonic decays is 0.2173(51). This combines experimental results with the D^+ decay constant determined in $N_f = 2+1+1$ lattice QCD by the Fermilab/MILC collaboration [5]. Another constraint follows from the ratio of D_s to D leptonic decay rates [66] combined with the ratio of D_s and D decay constants. Using ratios of $V_{cs} f_{D_s}$ and $V_{cd} f_{D^+}$ averaged over experimental results from [3] and the lattice QCD result for f_{D_s}/f_{D^+} from [5] gives the constraint $|V_{cd}|/|V_{cs}| = 0.2209(56)$ if we assume that electromagnetic corrections to the leptonic rates will largely cancel.

The black dashed line in Figure 23 corresponds to the unitarity constraint $|V_{cd}|^2 + |V_{cs}|^2 + |V_{cb}|^2 = 1$. V_{cb} has little impact on this curve; we use the average value of 0.0410(14) from [3]. Our result for V_{cs} is in good agreement with the unitarity curve for values of V_{cd} in the range given by the leptonic and semileptonic constraints.

Figure 24 gives the same picture for the V_{us}, V_{cs}, V_{ts} column of the CKM matrix, showing constraints in the $|V_{cs}| - |V_{us}|$ plane. $|V_{cs}|$ values are as for Figure 23 but plotted over a smaller range because of the higher accuracy of $|V_{us}|$ (we scale x and y axis ranges together).

We take $|V_{us}|$ values from the review 'V_{ud}, V_{us}, Cabibbo angle and CKM unitarity' in [3]. This gives $|V_{us}| = 0.2252(5)$ from leptonic decays of K^+ and 0.2231(7) from $K \to \pi$ semileptonic decay. The leptonic result uses an average [7] of lattice QCD results for the K decay constants dominated by that from [5]. The semileptonic result uses an average [7] of lattice QCD results for the $K \to \pi$ form factor at $q^2 = 0$ from [67, 68]. The current most accurate lattice QCD results for the form factor are given in [6].

Figure 24 shows the tension developing between leptonic and semileptonic determinations of V_{us} [3, 6]. The black dashed line in the figure shows the unitarity constraint $|V_{us}|^2 + |V_{cs}|^2 + |V_{ts}|^2 = 1$. $|V_{ts}|$ has little impact on this curve; we use the current most accurate determination of $|V_{ts}| = 0.04189(93)$ from the measured oscillation rate of B_s mesons [3] and HPQCD's lattice QCD determination [39] of the matrix elements of the 4-quark operators that give the mass difference between the B_s eigenstates. Our improved accuracy for $|V_{cs}|$, along with the unitarity curve, is not sufficient to distinguish be-

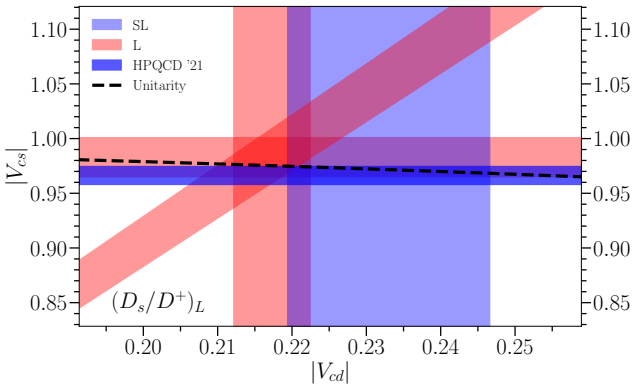

FIG. 23. A comparison of constraints on V_{cs} and V_{cd} with the expectation from CKM unitarity. Red bands show the $\pm1\sigma$ range for the determination of V_{cs} and V_{cd} from leptonic decays of D_s and D^+ combined with decay constants from lattice QCD. The diagonal red band is the constraint from the ratio of leptonic rates for D_s and D^+ combined with the lattice QCD ratio of decay constants. The solid light blue band shows the result for V_{cd} from the $D \to \pi\ell\overline{\nu}$ decay combined with lattice QCD form factor results. See the text for a discussion of the values used. The darker blue band shows our new determination here of V_{cs} from $D \to K\ell\overline{\nu}$ with $\pm1\sigma$ uncertainties. For comparison the black dashed line gives the unitarity constraint curve of $|V_{cd}|^2 + |V_{cs}|^2 + |V_{cb}|^2 = 1$.

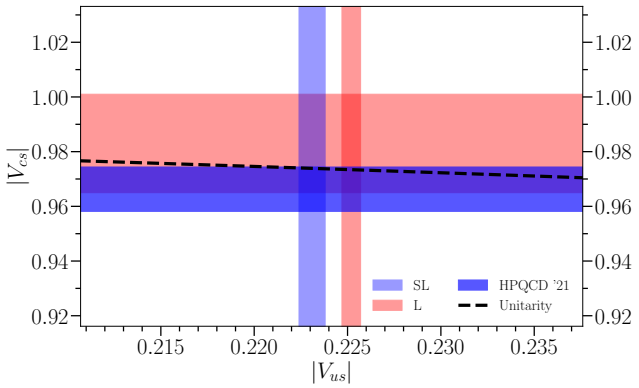

FIG. 24. A comparison of constraints on V_{cs} and V_{us} with the expectation from CKM unitarity. Red bands show the $\pm1\sigma$ range for the determination of V_{cs} and V_{us} from leptonic decays of D_s and K^+ combined with decay constants from lattice QCD. The light blue band shows the result for V_{us} from $K \to \pi\ell\overline{\nu}$ decay combined with lattice QCD form factor results. See the text for a discussion of the values used. The darker blue band shows our new determination here of V_{cs} from $D \to K\ell\overline{\nu}$ with $\pm1\sigma$ uncertainties. For comparison the black dashed line gives the unitarity constraint curve, $|V_{us}|^2 + |V_{cs}|^2 + |V_{ts}|^2 = 1$.

tween the two values for $|V_{us}|$.

VII. CONCLUSIONS

We have completed a detailed lattice QCD calculation of the scalar and vector form factors that parameterise the strong interaction effects in the $D \to K\ell\nu$ semileptonic decay process in the Standard Model. Our calculation covers the full physical range of momentum transfer. With high statistics on eight gluon field ensembles, three with physical light quarks, and a highly improved discretisation of QCD that allows nonperturbative normalisation of weak current operators, we have improved significantly on the precision of previous work.

In Table III we give the parameters, and their uncertainties and correlation matrix, that enable our form factors to be reconstructed. We give our form factor values at $q^2 = 0$ and $q^2_{\rm max}$ in Eq. (35). Our lattice QCD calculations use $m_u = m_d = m_l$; we take an additional 0.15% uncertainty on the form factors (uniformly in q^2) to allow for the impact of $m_u \neq m_d$ in the form factors when we compare to experimental results. Figure 10 compares the shape parameters for our form factors to those inferred from the experimental differential rate, and shows good agreement.

In Section IV B we give results for observables that allow tests of lepton flavour universality violation. These are the ratio of branching fractions for $D \to K\ell\nu$ decay for $\ell = \mu$ to that for $\ell = e$, $R_{\mu/e}$, and the lepton forward-backward asymmetry for the μ case (this quantity being very small for the e case). We obtain (repeating Eq. (37))

$$R_{\mu/e} = 0.9779(2)_{\rm latt}(50)_{\rm EM} \tag{47}$$

in the Standard Model, including an uncertainty for QED corrections of 0.5% for the $D^0 \to K^-$ case being studied by BES [57]. We show what the impact of a new physics coupling for muons could be in Figures 11 and 12.

Section V gives our new determinations of V_{cs} from combining experimental measurements with our form factors. We give three different methods based on using the differential decay rate, binned in q^2, using the total branching fraction and using experimental results extrapolated to $q^2 = 0$. The results we obtain (repeating Eqs. (43), (44) and (45)) are

$$\begin{aligned}
|V_{cs}|^{{\rm d}\Gamma/{\rm d}q^2} &= 0.9663(53)_{\rm latt}(39)_{\rm exp}(19)_{\eta_{EW}}(40)_{\rm EM} \\
|V_{cs}|^{\mathcal{B}} &= 0.9686(54)_{\rm latt}(39)_{\rm exp}(19)_{\eta_{EW}}(30)_{\rm EM} \\
|V_{cs}|^{f_+(0)} &= 0.9643(57)_{\rm latt}(44)_{\rm exp}(19)_{\eta_{EW}}(48)_{\rm EM}.
\end{aligned} \tag{48}$$

Our preferred result is the top one; adding uncertainties in quadrature this gives (repeating Eq. (46))

$$V_{cs} = 0.9663(80). \tag{49}$$

This total 0.83% uncertainty is a significant improvement (by a factor of two) on the previous most accurate result [20]. The uncertainty is reduced by a factor of four over the value from [3] quoted in Eq. (6) in Section I. This is the first time that a direct determination of V_{cs}

has been accurate enough to see a significant difference (over 4σ) from 1.

As discussed in Section I the limitation on the determination of V_{cs} from semileptonic decays (unlike for leptonic decay processes) was the accuracy of the lattice QCD calculation. Improving the accuracy of the form factors has then allowed us to leverage a significant improvement in the outcome for V_{cs}. There is still room for further improvement, as can be seen in Eq. (48). The lattice QCD uncertainty is still larger than that from experiment, but not by a large margin, so a reduction in the experimental uncertainty would also help. A significant source of uncertainty is from long-distance QED corrections to the $D \to K$ semileptonic process. Improved understanding of these is needed and new methods in lattice QCD+QED may help here [60]. Further improvements would include lattice calculations with $m_u \neq m_d$.

In Table IV we give the integrated total rates calculated from our form factors, $\Gamma/(|\eta_{EW}V_{cs}|^2(1+\delta_{EM}))$, for $D \to K$ semileptonic decay for the four different meson charge and lepton modes we consider here. These can be used with improved experimental determinations of the total branching fractions to improve $|V_{cs}|$ in the future, even if an improved determination of the differential rates is not available.

Finally, we update the second row and column unitarity tests using our new value for V_{cs} in Eq. (49) and results for other elements as given in Section VI and plotted in Figures 23 and 24. For the second row, using $V_{cd} = 0.2173(51)$ from leptonic D^+ decays and $V_{cb} = 0.0410(14)$ [3] we have

$$|V_{cd}|^2 + |V_{cs}|^2 + |V_{cb}|^2 = 0.9826(22)_{V_{cd}}(155)_{V_{cs}}(1)_{V_{cb}}. \quad (50)$$

For the second column, using a weighted average of leptonic and semileptonic values of V_{us} of 0.2245(4) [3] and $V_{ts} = 0.04189(93)$ [39] gives

$$|V_{us}|^2 + |V_{cs}|^2 + |V_{ts}|^2 = 0.9859(2)_{V_{us}}(155)_{V_{cs}}(1)_{V_{ts}}. \quad (51)$$

Both are in good agreement with the value of 1 for unitarity. Since the total uncertainty on the unitarity relation depends mainly on that from V_{cs}, our new result for $|V_{cs}|$ has enabled a very substantial improvement over earlier results, giving a total uncertainty on the unitarity tests of 1.6%.

Acknowledgements

We are grateful to the MILC collaboration for the use of their configurations and code. We thank R. Briere, A. Davis, J. Harrison, D. Hatton and M. Wingate for useful discussions. This work used the DiRAC Data Analytic system at the University of Cambridge, operated by the University of Cambridge High Performance Computing Service on behalf of the STFC DiRAC HPC Facility (www.dirac.ac.uk). This equipment was funded by BIS National E-infrastructure capital grant (ST/K001590/1), STFC capital grants ST/H008861/1 and ST/H00887X/1, and STFC DiRAC Operations grant ST/K00333X/1. DiRAC is part of the National E-Infrastructure. We are grateful to the Cambridge HPC support staff for assistance. Funding for this work came from the Gilmour bequest to the University of Glasgow, the Isaac Newton Trust, the Leverhulme Trust ECF scheme, the National Science Foundation and the Science and Technology Facilities Council.

TABLE V. Priors used in the fit on each set. $d^H_{i\neq 0}$ ($H = D/K$) indicates the amplitudes for normal and oscillating D mesons and for normal K mesons. $d_i^{K,o}$ is the amplitude for oscillating K, which we expect to be smaller because the oscillation vanishes at zero momentum when the quark masses are the same. Parameters denoted S and V refer to the J^{kl}_{ij} parameters for the scalar and temporal vector currents respectively. Columns 4 and 5 then give the priors for the ground-state to ground-state parameter cases where at least one of the states is an oscillating state. For the cases where at least one state is an excited state, $\mathcal{P}[S^{kl}_{ij\neq 00}] = \mathcal{P}[V^{kl}_{ij\neq 00}] = 0.0(5)$ in all cases.

set	$\mathcal{P}[d^D_{i\neq 0}]$	$\mathcal{P}[d_i^{K,o}]$	$\mathcal{P}[S_{00}^{kl\neq nn}]$	$\mathcal{P}[V_{00}^{kl\neq nn}]$
1	0.15(20)	0.05(5)	0.0(1.0)	0.0(1.0)
2	0.15(10)	0.05(5)	0.0(1.0)	0.0(1.0)
3	0.10(10)	0.05(5)	0.0(1.5)	0.0(1.5)
4	0.20(20)	0.05(5)	0.0(1.5)	0.0(1.5)
5	0.20(20)	0.03(3)	0.0(1.0)	0.0(1.0)
6	0.10(10)	0.05(5)	0.0(1.5)	0.0(1.5)
7	0.05(5)	0.02(2)	0.0(1.0)	0.0(2.0)
8	0.08(10)	0.01(2)	0.0(1.0)	0.0(1.5)

Appendix A: Correlator Fits: further details and results

The fits to the correlators that we calculate in lattice QCD are described in Section III C. Here we give more details of prior choices for the fit parameters, give the table of results for ground-state parameters and illustrate some of the tests of the fit results.

Section III C discusses how the priors for ground-state energies and two- and three-point amplitudes can be estimated from the correlators. Table V gives the prior values that we use for excited state amplitudes for non-oscillating and oscillating states. It also lists the priors for the three-point parameters J^{pq}_{00} (see Eq. (20)) for the case where pq includes oscillating states. The priors for J^{pq}_{ij} when $ij \neq 00$ are 0.0(5) in all cases.

Table VI gives the ground-state parameters from our preferred fit to the correlators for each gluon field ensemble. Columns 8 and 9 of the table give the results

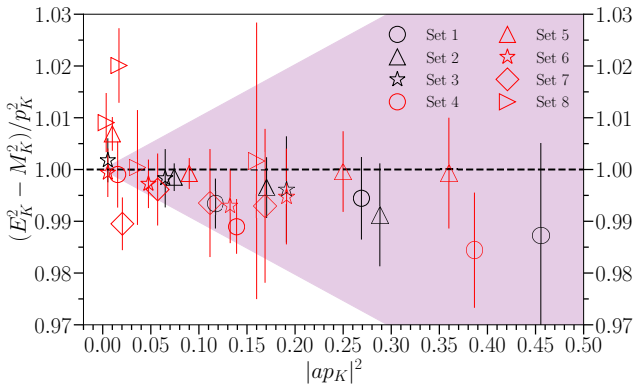

FIG. 25. For each ensemble, we plot the ratio $(E_K^2 - M_K^2)/|\vec{p}_K|^2$ from our fit results against $|a\vec{p}_K|^2$ to check that the K meson energy agrees with that expected from the spatial momentum given to the meson in the lattice calculation. The points for gluon field configurations with physical sea u/d quark mass are in black. The ratio agrees with the expected value of 1 throughout the range of momenta and lattice spacing values. The purple wedge shows $1 \pm |a\vec{p}_K/\pi|^2$.

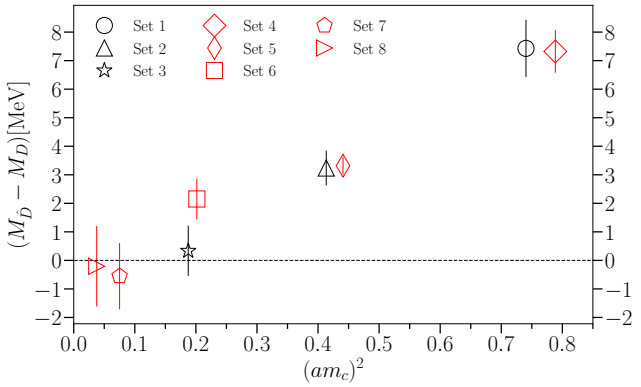

FIG. 26. The difference between the non-Goldstone $\hat{D}$ and Goldstone D meson masses, from our fit results, as a function of lattice spacing. The points in black are for gluon field configurations with physical u/d sea quark mass. The results show clearly that the splitting is a discretisation effect and is only a few MeV even on the coarsest lattices.

for the scalar and vector form factors determined from the matrix elements as described in Section II. These are given as a function of q^2 in lattice units where q^2 is determined from the D and K meson masses and the input lattice spatial momentum for the K. The results for the form factors on a given gluon field ensemble are correlated through our fit. We preserve those correlations through to the next stage of the fit where we determine the physical curve with uncertainty bands for $f_+(q^2)$ and $f_0(q^2)$, as described in Section III D.

A test of our fit results, plotted in Figure 25, is to work out the 'speed of light' from the energy and mass of the K meson at the different values of spatial momenta that we use. Our results show no significant disagreement with

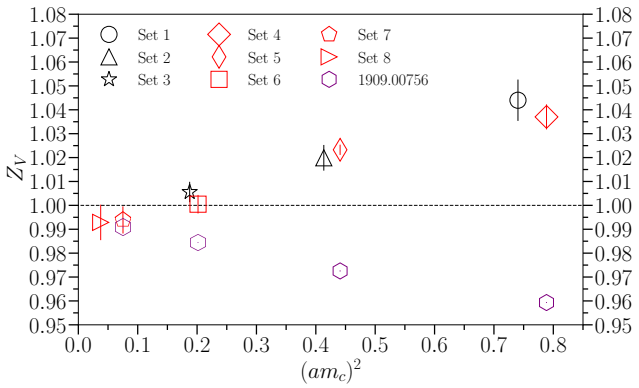

FIG. 27. The renormalisation factor for the local temporal vector current, Z_V, plotted as a function of lattice spacing. The points in black correspond to gluon field configurations with physical u/d sea quark mass. The purple hexagons give results for Z_V values for the local vector current determined in a symmetric momentum-subtraction scheme on the lattice [26]. The two sets of Z_V values differ at finite lattice spacing by discretisation effects.

the result of one expected from relativity at the ≈1% level of our statistical errors in this quantity. There is no sign of significant discretisation effects.

Figure 26 shows the mass difference between the Goldstone D meson and the nonGoldstone D meson (denoted $\hat{D}$) that we use in the temporal vector three-point correlation functions. We see that the difference in mass is, as expected, a discretisation effect, vanishing as $a \to 0$. This shows that any effects in our form factors from this mass difference are easily taken care of in the discretisation effects that we allow in our extrapolation of the form factors to the $a \to 0$ limit.

Figure 27 plots our results for the renormalisation factor for the temporal vector current, Z_V. This is determined from the matrix elements of the scalar and temporal vector currents when both the D and K are at rest (zero recoil) from Eq. (13). Since this renormalisation constant matches the lattice regularisation of QCD to that in the continuum for a current with no anomalous dimensions, it takes the form of a perturbative series in α_s, up to discretisation effects. Our results for Z_V are very similar, not surprisingly, to those determined for the $c\bar{s}$ temporal vector current in $B_c \to B_s$ decays in [69]. In that paper a comparison was made to the results for an $s\bar{s}$ current in [70] where Z_V was shown to have the expected behaviour. The comparison in [69] shows that the results for Z_V for $c\bar{s}$ and $s\bar{s}$ differ only by discretisation effects.

Another way to determine Z_V is using a symmetric momentum-subtraction scheme, known as RI-SMOM, on the lattice. In Figure 27 we compare results for Z_V for the local vector current determined this way from [26], taking values at $\mu = 2$ GeV. These Z_V values differ from the ones used here by discretisation effects. Hence, as in the paragraph above, we conclude that using a different

TABLE VI. Ground-state parameters determined from our correlator fits for each gluon field ensemble.Columns 3 and 5 give the ground-state D Goldstone meson mass and K energy in lattice units, for the q^2 value given in lattice units in Column 4. Columns 6 and 7 give the matrix elements between D and K of the local scalar current and the local temporal vector current (*before* multiplication with Z_V given in column 10 (and determined from Eq. (13)). Columns 8 and 9 give the scalar and vector form factors (determined from Eqs. (10) and (11)).

set	$am_c^{\rm val}$	aM_D	$(aq)^2$	aE_K	$\langle K\vert\, S\,\vert D\rangle$	$\langle K\vert\, V^0_{\rm latt}\,\vert \hat{D}\rangle$	$f_0(q^2)$	$f_+(q^2)$	Z_V
1	0.8605	1.44857(46)	1.1443(10)	0.37886(17)	2.524(13)	1.792(16)	1.0236(49)		1.0440(87)
			0.76263(88)	0.51059(13)	2.236(12)	1.605(14)	0.9066(46)	1.133(29)	
			0.38113(75)	0.64227(10)	2.033(18)	1.480(21)	0.8243(72)	0.912(14)	
			-0.00042(62)	0.773970(85)	1.861(54)	1.425(59)	0.755(22)	0.755(22)	
2	0.643	1.15450(30)	0.72338(50)	0.303983(49)	2.1519(74)	1.4643(83)	1.0240(31)		1.0199(54)
			0.48244(44)	0.408334(36)	1.9015(60)	1.3104(68)	0.9049(26)	1.123(13)	
			0.24166(38)	0.512611(29)	1.713(10)	1.193(11)	0.8154(49)	0.9029(90)	
			0.00092(32)	0.616870(24)	1.561(21)	1.093(22)	0.7428(98)	0.7430(98)	
3	0.433	0.83391(27)	0.37853(32)	0.218659(54)	1.6558(46)	1.0625(46)	1.0151(24)		1.0056(43)
			0.35885(32)	0.230461(51)	1.6207(44)	1.0435(47)	0.9935(24)	1.32(15)	
			0.18311(26)	0.335833(35)	1.3707(71)	0.8967(80)	0.8403(44)	0.977(15)	
			-0.07179(18)	0.488663(24)	1.123(24)	0.769(25)	0.689(15)	0.658(14)	
4	0.888	1.49339(36)	1.16033(71)	0.41621(17)	2.5532(58)	1.868(10)	1.0147(20)		1.0370(52)
			1.10578(70)	0.43447(16)	2.5090(54)	1.8355(97)	0.9971(18)	1.45(11)	
			0.73402(62)	0.55894(13)	2.2457(94)	1.661(12)	0.8925(37)	1.086(18)	
			0.16891(50)	0.748140(96)	1.966(30)	1.523(36)	0.781(12)	0.806(14)	
5	0.664	1.19124(20)	0.73636(31)	0.333122(92)	2.1645(32)	1.5025(35)	1.0086(13)		1.0233(21)
			0.70138(30)	0.347804(88)	2.1261(30)	1.4756(33)	0.9906(12)	1.426(48)	
			0.46203(27)	0.448268(68)	1.9069(40)	1.3325(41)	0.8885(18)	1.0896(75)	
			0.09875(22)	0.600748(51)	1.688(16)	1.187(15)	0.7867(75)	0.8191(86)	
			-0.10483(19)	0.686198(45)	1.571(23)	1.109(21)	0.732(11)	0.7029(97)	
6	0.449	0.86434(23)	0.38678(26)	0.24243(10)	1.6898(37)	1.1173(47)	1.0100(19)		1.0005(39)
			0.36829(26)	0.253122(99)	1.6594(36)	1.0978(46)	0.9918(19)	1.39(11)	
			0.24226(23)	0.326027(77)	1.4791(59)	0.9796(73)	0.8841(35)	1.097(21)	
			0.04974(18)	0.437394(57)	1.282(11)	0.875(12)	0.7661(64)	0.7926(73)	
			-0.05805(16)	0.499751(50)	1.222(27)	0.879(34)	0.731(16)	0.710(16)	
7	0.274	0.56711(21)	0.16562(16)	0.160142(78)	1.1898(39)	0.7371(45)	1.0074(30)		0.9940(56)
			0.10378(14)	0.214663(59)	1.0429(45)	0.6534(54)	0.8830(37)	1.066(24)	
			0.02098(11)	0.287665(44)	0.920(14)	0.584(18)	0.779(12)	0.806(13)	
			-0.072829(79)	0.370376(34)	0.809(21)	0.516(22)	0.685(18)	0.610(18)	
			-0.152857(51)	0.440934(29)	0.733(35)	0.497(33)	0.621(29)	0.515(29)	
8	0.194	0.42167(21)	0.09183(12)	0.118624(77)	0.9325(40)	0.5501(44)	1.0109(38)		0.9929(74)
			0.07976(11)	0.132947(69)	0.8900(36)	0.5284(43)	0.9648(35)	1.241(66)	
			0.043459(98)	0.175987(52)	0.7804(44)	0.4683(48)	0.8460(46)	0.970(15)	
			0.002959(79)	0.224011(41)	0.6795(88)	0.4182(94)	0.7366(96)	0.7425(99)	
			-0.1600027(18)	0.417246(22)	0.566(95)	0.338(72)	0.61(10)	0.401(84)	

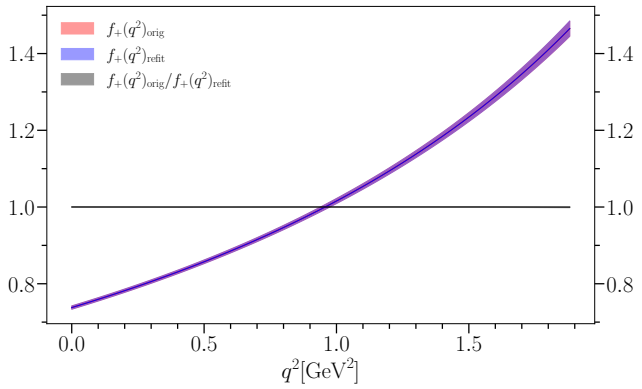

FIG. 28. The original f_+ form factor, as well as the result using the refitting procedure described here. The black line (and grey uncertainty band, barely visible) is the ratio of the two. We see that the refitting reproduces the original form factor and its uncertainty accurately.

prescription for Z_V would give the same results in the continuum limit.

Appendix B: Obtaining parameters for the z-expansion fit form used by experiments

We can compare the shape of our vector form factor to that inferred from the experimental differential rate by comparing the parameters obtained from z-expansion fit. To do this we must use the same q^2 to z mapping and the same form for the z-expansion as that used by the experiments. This form is

$$f_+(q^2) = \frac{1}{z(q^2, t_0 = M_{D_s^*}^2)\phi(q^2)} \sum_{n=0}^{N-1} a_n^+ z^n, \tag{B1}$$

where the outer function,

$$\phi(q^2, t_0) = \sqrt{\frac{\pi}{3}} m_c \left(\frac{z(q^2,0)}{-q^2}\right)^{5/2} \left(\frac{z(q^2,t_0)}{t_0 - q^2}\right)^{-1/2} \times \left(\frac{z(q^2,t_-)}{t_- - q^2}\right)^{-3/4} \frac{t_+ - q^2}{(t_+ - t_0)^{1/4}}. \tag{B2}$$

The q^2 to z mapping (see Eq. (23)) uses $t_0 = t_+(1 - (1 - t_-/t_+)^{1/2})$ (for $t_{+/-} = (M_D \pm M_K)^2$). This is the prescription that minimises the maximum value of z over the q^2 range of the decay. The parameter $m_c = 1.25$GeV.

We apply the fit form of Eq. (B1) to our form factors at the physical point, generating synthetic data from Table III. We used 20 evenly spaced points but changing the number of points makes no difference. This gives us the parameters a_n^+ for this fit form, along with their correlation matrix and these are the values plotted in Figure 10.

Figure 28 compares our original vector form factor and the refitted one and also plots the ratio of the two. This confirms that our refitting process does not change the form factor or its uncertainty, but is simply a convenient way to determine the parameters of Eq. (B1) for comparison to experiment.

[1] Nicola Cabibbo, "Unitary Symmetry and Leptonic Decays," *Meeting of the Italian School of Physics and Weak Interactions Bologna, Italy, April 26-28, 1984*, Phys. Rev. Lett. **10**, 531–533 (1963), [,648(1963)].

[2] Makoto Kobayashi and Toshihide Maskawa, "CP Violation in the Renormalizable Theory of Weak Interaction," Prog. Theor. Phys. **49**, 652–657 (1973).

[3] P.A. Zyla *et al.* (Particle Data Group), "Review of Particle Physics," PTEP **2020**, 083C01 (2020).

[4] Matthew Wingate, "Quark flavor physics and lattice QCD," in *38th International Symposium on Lattice Field Theory* (2020) arXiv:2103.17224 [hep-lat].

[5] A. Bazavov *et al.*, "B- and D-meson leptonic decay constants from four-flavor lattice QCD," Phys. Rev. **D98**, 074512 (2018), arXiv:1712.09262 [hep-lat].

[6] A. Bazavov *et al.* (Fermilab Lattice, MILC), "$|V_{us}|$ from $K_{\ell 3}$ decay and four-flavor lattice QCD," Phys. Rev. D **99**, 114509 (2019), arXiv:1809.02827 [hep-lat].

[7] S. Aoki *et al.* (Flavour Lattice Averaging Group), "FLAG Review 2019," Eur. Phys. J. **C80**, 113 (2020), arXiv:1902.08191 [hep-lat].

[8] G. C. Donald, C. T. H. Davies, J. Koponen, and G. P. Lepage (HPQCD), "V_{cs} from $D_s \to \phi\ell\nu$ semileptonic decay and full lattice QCD," Phys. Rev. **D90**, 074506 (2014), arXiv:1311.6669 [hep-lat].

[9] Stefan Meinel, "$\Lambda_c \to \Lambda l^+ \nu_l$ form factors and decay rates from lattice QCD with physical quark masses," Phys. Rev. Lett. **118**, 082001 (2017), arXiv:1611.09696 [hep-lat].

[10] Yasmine Sara Amhis *et al.* (HFLAV), "Averages of b-hadron, c-hadron, and τ-lepton properties as of 2018," (2019), arXiv:1909.12524 [hep-ex].

[11] Piotr Golonka and Zbigniew Was, "PHOTOS Monte Carlo: A Precision tool for QED corrections in Z and W decays," Eur. Phys. J. C **45**, 97–107 (2006), arXiv:hep-ph/0506026.

[12] Bogdan A. Dobrescu and Andreas S. Kronfeld, "Accumulating evidence for nonstandard leptonic decays of D_s mesons," Phys. Rev. Lett. **100**, 241802 (2008), arXiv:0803.0512 [hep-ph].

[13] A. Sirlin, "Large m(W), m(Z) Behavior of the O(alpha) Corrections to Semileptonic Processes Mediated by W," Nucl. Phys. B **196**, 83–92 (1982).

[14] C. Aubin *et al.*, "Charmed meson decay constants in three-flavor lattice QCD," Phys. Rev. Lett. **95**, 122002 (2005), arXiv:hep-lat/0506030.

[15] E. Follana, Q. Mason, C. Davies, K. Hornbostel, G.P. Lepage, J. Shigemitsu, H. Trottier, and K. Wong (HPQCD, UKQCD), "Highly improved staggered quarks on the lattice, with applications to charm physics," Phys.

Rev. D **75**, 054502 (2007), arXiv:hep-lat/0610092.
[16] E. Follana, C.T.H. Davies, G.P. Lepage, and J. Shigemitsu (HPQCD, UKQCD), "High Precision determination of the pi, K, D and D(s) decay constants from lattice QCD," Phys. Rev. Lett. **100**, 062002 (2008), arXiv:0706.1726 [hep-lat].
[17] C.T.H. Davies, C. McNeile, E. Follana, G.P. Lepage, H. Na, and J. Shigemitsu (HPQCD), "Update: Precision D_s decay constant from full lattice QCD using very fine lattices," Phys. Rev. D **82**, 114504 (2010), arXiv:1008.4018 [hep-lat].
[18] C. Aubin *et al.* (Fermilab Lattice, MILC, HPQCD), "Semileptonic decays of D mesons in three-flavor lattice QCD," Phys. Rev. Lett. **94**, 011601 (2005), arXiv:hep-ph/0408306.
[19] Heechang Na, Christine T. H. Davies, Eduardo Follana, G. Peter Lepage, and Junko Shigemitsu (HPQCD), "The $D \to K, l\nu$ Semileptonic Decay Scalar Form Factor and $|V_{cs}|$ from Lattice QCD," Phys. Rev. **D82**, 114506 (2010), arXiv:1008.4562 [hep-lat].
[20] J. Koponen, C. T. H. Davies, G. C. Donald, E. Follana, G. P. Lepage, H. Na, and J. Shigemitsu (HPQCD), "The shape of the $D \to K$ semileptonic form factor from full lattice QCD and V_{cs}," (2013), arXiv:1305.1462 [hep-lat].
[21] V. Lubicz, L. Riggio, G. Salerno, S. Simula, and C. Tarantino (ETM), "Scalar and vector form factors of $D \to \pi(K)\ell\nu$ decays with $N_f = 2 + 1 + 1$ twisted fermions," Phys. Rev. **D96**, 054514 (2017), [erratum: Phys. Rev.D99,no.9,099902(2019); Erratum: Phys. Rev.D100,no.7,079901(2019)], arXiv:1706.03017 [hep-lat].
[22] L. Riggio, G. Salerno, and S. Simula, "Extraction of $|V_{cd}|$ and $|V_{cs}|$ from experimental decay rates using lattice QCD $D \to \pi(K)\ell\nu$ form factors," Eur. Phys. J. C **78**, 501 (2018), arXiv:1706.03657 [hep-lat].
[23] T. Kaneko, B. Fahy, H. Fukaya, and S. Hashimoto (JLQCD), "D meson semileptonic decays in lattice QCD with Moebius domain-wall quarks," PoS **LATTICE2016**, 297 (2017), arXiv:1701.00942 [hep-lat].
[24] Ruizi Li *et al.* (Fermilab Lattice, MILC), "D meson Semileptonic Decay Form Factors at $q^2 = 0$," PoS **LATTICE2018**, 269 (2019), arXiv:1901.08989 [hep-lat].
[25] W. Altmannshofer *et al.* (Belle-II), "The Belle II Physics Book," PTEP **2019**, 123C01 (2019), [Erratum: PTEP 2020, 029201 (2020)], arXiv:1808.10567 [hep-ex].
[26] D. Hatton, C.T.H. Davies, G.P. Lepage, and A.T. Lytle (HPQCD), "Renormalizing vector currents in lattice QCD using momentum-subtraction schemes," Phys. Rev. D **100**, 114513 (2019), arXiv:1909.00756 [hep-lat].
[27] Szabolcs Borsanyi *et al.*, "High-precision scale setting in lattice QCD," JHEP **09**, 010 (2012), arXiv:1203.4469 [hep-lat].
[28] R. J. Dowdall, C. T. H. Davies, G. P. Lepage, and C. McNeile (HPQCD), "Vus from pi and K decay constants in full lattice QCD with physical u, d, s and c quarks," Phys. Rev. **D88**, 074504 (2013), arXiv:1303.1670 [hep-lat].
[29] Christopher Monahan, Junko Shigemitsu, and Ron Horgan, "Matching lattice and continuum axial-vector and vector currents with nonrelativistic QCD and highly improved staggered quarks," Phys. Rev. **D87**, 034017 (2013), arXiv:1211.6966 [hep-lat].
[30] A. Bazavov *et al.* (MILC), "Lattice QCD Ensembles with Four Flavors of Highly Improved Staggered Quarks," Phys. Rev. D **87**, 054505 (2013), arXiv:1212.4768 [hep-lat].
[31] A. Hart, G. M. von Hippel, and R. R. Horgan (HPQCD), "Radiative corrections to the lattice gluon action for HISQ improved staggered quarks and the effect of such corrections on the static potential," Phys. Rev. **D79**, 074008 (2009), arXiv:0812.0503 [hep-lat].
[32] D. Guadagnoli, F. Mescia, and S. Simula, "Lattice study of semileptonic form-factors with twisted boundary conditions," Phys. Rev. **D73**, 114504 (2006), arXiv:hep-lat/0512020 [hep-lat].
[33] E. McLean, C.T.H. Davies, J. Koponen, and A.T. Lytle (HPQCD), "$B_s \to D_s\ell\nu$ Form Factors for the full q^2 range from Lattice QCD with non-perturbatively normalized currents," Phys. Rev. D **101**, 074513 (2020), arXiv:1906.00701 [hep-lat].
[34] W. G. Parrott, C. Bouchard, C. T. H. Davies, and D. Hatton (HPQCD), "Toward accurate form factors for B-to-light meson decay from lattice QCD," Phys. Rev. D **103**, 094506 (2021), arXiv:2010.07980 [hep-lat].
[35] G. P. Lepage, B. Clark, C. T. H. Davies, K. Hornbostel, P. B. Mackenzie, C. Morningstar, and H. Trottier, "Constrained curve fitting," *Lattice field theory. Proceedings, 19th International Symposium, Lattice 2001, Berlin, Germany, August 19-24, 2001*, Nucl. Phys. Proc. Suppl. **106**, 12–20 (2002), arXiv:hep-lat/0110175 [hep-lat].
[36] Peter Lepage and Christoph Gohlke, "gplepage/lsqfit: lsqfit version 11.5.1," (2020).
[37] Peter Lepage, Christoph Gohlke, and Daniel Hackett, "gplepage/gvar: gvar version 11.2," (2020).
[38] Peter Lepage, "gplepage/corrfitter: corrfitter version 8.0.3," (2019).
[39] R. J. Dowdall, C. T. H. Davies, R. R. Horgan, G. P. Lepage, C. J. Monahan, J. Shigemitsu, and M. Wingate (HPQCD), "Neutral B-meson mixing from full lattice QCD at the physical point," Phys. Rev. D **100**, 094508 (2019), arXiv:1907.01025 [hep-lat].
[40] Richard J. Hill, "The Modern description of semileptonic meson form factors," *Proceedings, 4th Conference on Flavor Physics and CP Violation (FPCP 2006): Vancouver, British Columbia, Canada, April 9-12, 2006*, eConf **C060409**, 027 (2006), arXiv:hep-ph/0606023 [hep-ph].
[41] Claude Bourrely, Irinel Caprini, and Laurent Lellouch, "Model-independent description of $B \to \pi\ell\nu$ decays and a determination of $|V(ub)|$," Phys. Rev. **D79**, 013008 (2009), [Erratum: Phys. Rev.D82,099902(2010)], arXiv:0807.2722 [hep-ph].
[42] C. T. H. Davies, E. Follana, I. D. Kendall, G. Peter Lepage, and C. McNeile (HPQCD), "Precise determination of the lattice spacing in full lattice QCD," Phys. Rev. D **81**, 034506 (2010), arXiv:0910.1229 [hep-lat].
[43] Bipasha Chakraborty, C. T. H. Davies, B. Galloway, P. Knecht, J. Koponen, G. C. Donald, R. J. Dowdall, G. P. Lepage, and C. McNeile (HPQCD), "High-precision quark masses and QCD coupling from $n_f = 4$ lattice QCD," Phys. Rev. **D91**, 054508 (2015), arXiv:1408.4169 [hep-lat].
[44] D. Hatton, C. T. H. Davies, B. Galloway, J. Koponen, G. P. Lepage, and A. T. Lytle (HPQCD), "Charmonium properties from lattice QCD+QED : Hyperfine splitting, J/ψ leptonic width, charm quark mass, and a^c_μ," Phys. Rev. D **102**, 054511 (2020), arXiv:2005.01845 [hep-lat].
[45] Johan Bijnens and Ilaria Jemos, "Vector Formfactors in Hard Pion Chiral Perturbation Theory," Nucl. Phys. B

846, 145–166 (2011), arXiv:1011.6531 [hep-ph].
[46] C. M. Bouchard, G. Peter Lepage, Christopher Monahan, Heechang Na, and Junko Shigemitsu (HPQCD), "$B_s \to K\ell\nu$ form factors from lattice QCD," Phys. Rev. **D90**, 054506 (2014), arXiv:1406.2279 [hep-lat].
[47] C. Bernard (MILC), "Chiral logs in the presence of staggered flavor symmetry breaking," Phys. Rev. D **65**, 054031 (2002), arXiv:hep-lat/0111051.
[48] J.P. Lees *et al.* (BaBar), "Measurement of the $D^*(2010)^+$ natural line width and the $D^*(2010)^+ - D^0$ mass difference," Phys. Rev. D **88**, 052003 (2013), [Erratum: Phys.Rev.D 88, 079902 (2013)], arXiv:1304.5009 [hep-ex].
[49] M. Steffen, "A simple method for monotonic interpolation in one dimension," Astron. Astrophys. **239**, 443–450 (1990).
[50] D. Besson *et al.* (CLEO), "Improved measurements of D meson semileptonic decays to pi and K mesons," Phys. Rev. D **80**, 032005 (2009), arXiv:0906.2983 [hep-ex].
[51] Bernard Aubert *et al.* (BaBar), "Measurement of the hadronic form-factor in $D^0 \to K^- e^+ \nu_e$ 1," Phys. Rev. D **76**, 052005 (2007), arXiv:0704.0020 [hep-ex].
[52] M. Ablikim *et al.* (BESIII), "Study of Dynamics of $D^0 \to K^- e^+ \nu_e$ and $D^0 \to \pi^- e^+ \nu_e$ Decays," Phys. Rev. D **92**, 072012 (2015), arXiv:1508.07560 [hep-ex].
[53] Y. Amhis *et al.* (HFLAV), "Averages of b-hadron, c-hadron, and τ-lepton properties as of summer 2016," Eur. Phys. J. C **77**, 895 (2017), arXiv:1612.07233 [hep-ex].
[54] Simone Bifani, Sébastien Descotes-Genon, Antonio Romero Vidal, and Marie-Hélène Schune, "Review of Lepton Universality tests in B decays," J. Phys. G **46**, 023001 (2019), arXiv:1809.06229 [hep-ex].
[55] Svjetlana Fajfer, Ivan Nisandzic, and Ursa Rojec, "Discerning new physics in charm meson leptonic and semileptonic decays," Phys. Rev. D **91**, 094009 (2015), arXiv:1502.07488 [hep-ph].
[56] Robert Fleischer, Ruben Jaarsma, and Gabriël Koole, "Testing Lepton Flavour Universality with (Semi)-Leptonic $D_{(s)}$ Decays," Eur. Phys. J. C **80**, 153 (2020), arXiv:1912.08641 [hep-ph].
[57] Medina Ablikim *et al.* (BESIII), "Study of the $D^0 \to K^- \mu^+ \nu_\mu$ dynamics and test of lepton flavor universality with $D^0 \to K^- \ell^+ \nu_\ell$ decays," Phys. Rev. Lett. **122**, 011804 (2019), arXiv:1810.03127 [hep-ex].
[58] Elisabetta Barberio and Zbigniew Was, "PHOTOS: A Universal Monte Carlo for QED radiative corrections. Version 2.0," Comput. Phys. Commun. **79**, 291–308 (1994).
[59] M. Antonelli *et al.* (FlaviaNet Working Group on Kaon Decays), "An Evaluation of $|V_{us}|$ and precise tests of the Standard Model from world data on leptonic and semileptonic kaon decays," Eur. Phys. J. C **69**, 399–424 (2010), arXiv:1005.2323 [hep-ph].
[60] C. T. Sachrajda, Matteo Di Carlo, Guido Martinelli, Davide Giusti, Vittorio Lubicz, Francesco Sanfilippo, Silvano Simula, and Nazario Tantalo, "Radiative corrections to semileptonic decay rates," PoS **LATTICE2019**, 162 (2019), arXiv:1910.07342 [hep-lat].
[61] M. Ablikim *et al.* (BESIII), "Analysis of $D^+ \to \bar{K}^0 e^+ \nu_e$ and $D^+ \to \pi^0 e^+ \nu_e$ semileptonic decays," Phys. Rev. D **96**, 012002 (2017), arXiv:1703.09084 [hep-ex].
[62] L. Widhalm *et al.* (Belle), "Measurement of D0 —¿ pi l nu (Kl nu) Form Factors and Absolute Branching Fractions," Phys. Rev. Lett. **97**, 061804 (2006), arXiv:hep-ex/0604049 [hep-ex].
[63] Medina Ablikim *et al.* (BESIII), "Improved measurement of the absolute branching fraction of $D^+ \to \bar{K}^0 \mu^+ \nu_\mu$," Eur. Phys. J. C **76**, 369 (2016), arXiv:1605.00068 [hep-ex].
[64] Medina Ablikim *et al.* (BESIII), "Determination of the absolute branching fractions of $D^0 \to K^- e^+ \nu_e$ and $D^+ \to \bar{K}^0 e^+ \nu_e$," (2021), arXiv:2104.08081 [hep-ex].
[65] M. Ablikim *et al.* (BESIII), "Study of decay dynamics and CP asymmetry in $D^+ \to K_L^0 e^+ \nu_e$ decay," Phys. Rev. D **92**, 112008 (2015), arXiv:1510.00308 [hep-ex].
[66] Peter A. Boyle, Luigi Del Debbio, Nicolas Garron, Andreas Juttner, Amarjit Soni, Justus Tobias Tsang, and Oliver Witzel (RBC/UKQCD), "SU(3)-breaking ratios for $D_{(s)}$ and $B_{(s)}$ mesons," (2018), arXiv:1812.08791 [hep-lat].
[67] A. Bazavov *et al.*, "Determination of $|V_{us}|$ from a Lattice-QCD Calculation of the $K \to \pi\ell\nu$ Semileptonic Form Factor with Physical Quark Masses," Phys. Rev. Lett. **112**, 112001 (2014), arXiv:1312.1228 [hep-ph].
[68] N. Carrasco, P. Lami, V. Lubicz, L. Riggio, S. Simula, and C. Tarantino, "$K \to \pi$ semileptonic form factors with $N_f = 2 + 1 + 1$ twisted mass fermions," Phys. Rev. D **93**, 114512 (2016), arXiv:1602.04113 [hep-lat].
[69] Laurence J. Cooper, Christine T. H. Davies, Judd Harrison, Javad Komijani, and Matthew Wingate (HPQCD), "$B_c \to B_{s(d)}$ form factors from lattice QCD," Phys. Rev. D **102**, 014513 (2020), arXiv:2003.00914 [hep-lat].
[70] Bipasha Chakraborty, C. T. H. Davies, G. C. Donald, J. Koponen, and G. P. Lepage (HPQCD), "Nonperturbative comparison of clover and highly improved staggered quarks in lattice QCD and the properties of the ϕ meson," Phys. Rev. D **96**, 074502 (2017), arXiv:1703.05552 [hep-lat].